

Mapping the 3-D dark matter with weak lensing in COMBO-17

A.N. Taylor^{1*}, D.J. Bacon^{1*}, M.E. Gray^{1*}, C. Wolf², K. Meisenheimer³, S. Dye⁴,
A. Borch³, M. Kleinheinrich³, Z. Kovacs³, L. Wisotzki⁵

¹*Institute for Astronomy, School of Physics, University of Edinburgh, Royal Observatory, Blackford Hill, Edinburgh, EH9 3HJ, U.K.*

²*Department of Physics, University of Oxford, Keble Road, Oxford OX1 3RH, U.K.*

³*Max-Planck-Institut für Astronomie, Königstuhl 17, D-69117, Heidelberg, Germany*

⁴*Astrophysics Group, Blackett Laboratory, Imperial College, Prince Consort Road, London SW7 2BW, U.K.*

⁵*Astrophysikalisches Institut Potsdam, An der Sternwarte 16, D-14482 Potsdam, Germany*

*email: ant@roe.ac.uk; djb@roe.ac.uk; meg@roe.ac.uk

ABSTRACT

We present a 3-dimensional lensing analysis of the $z = 0.16$ supercluster A901/2, resulting in a 3-D map of the dark matter distribution within a $3 \times 10^5 [h^{-1}\text{Mpc}]^3$ volume. This map is generated from a combined catalogue of 3-D galaxy coordinates together with shear estimates, using R -band imaging and photometric redshifts from the COMBO-17 survey. To estimate the 3-D positions and masses of the main clusters in the supercluster from lensing alone, we perform a χ^2 -fit of isothermal spheres to the tangential shear pattern around each cluster as a function of redshift. Motivated by the appearance of a second cluster behind A902 in galaxy number density, we also fit a two-cluster model to A902.

We then present the first 3-D map of the dark matter gravitational potential field, Φ , using the Kaiser-Squires (1993) and Taylor (2001) inversion methods. These maps clearly show the potential wells of the main supercluster components, including the new cluster behind A902, and demonstrates the applicability of 3-D dark matter mapping and projection free-mass-selected cluster finding to current data. Finally, we develop the halo model of dark matter and galaxy clustering and compare this with the auto- and cross-correlation functions of the 3-D gravitational potential, galaxy number densities and galaxy luminosity densities measured in the A901/2 field. We find significant anti-correlations between the gravitational potential field and the galaxy number density and luminosities, as expected due to baryonic infall into dark matter concentrations. We find good agreement with the halo model for the number densities and luminosity correlation functions, but some disagreement with the shape of the gravitational potential correlation function, which we attribute to finite-field effects.

Key words: Gravitation; gravitational lensing; Cosmology: observations, Dark Matter, Large-Scale Structure of Universe

1 INTRODUCTION

Gravitational lensing is a valuable method for measuring the matter distribution in the Universe (see e.g. Mellier 1999, Bartelmann & Schneider 2001). Light rays are deflected by the gravitational potential along their paths causing distortions in the shapes of background galaxies together with a change in their local number counts. These measurables are sensitive to all forms of matter, whether visible or dark, which brings gravitational lensing to the fore in studies of non-baryonic matter in the Universe. For most regions of the sky, observations of shape distortions (shear) reveal that the phenomenon is very weak ($\approx 1\%$ change in ellipticity of an

object). However we are still able to measure this effect by averaging the ellipticity of many galaxies to overcome the random intrinsic ellipticity of galaxies.

Many studies have used weak shear measurements to measure the two dimensional projected matter distribution of regions of space. This has led to precise understanding of the masses and mass profiles of galaxy clusters (see e.g. Tyson et al 1990, Kaiser & Squires 1993, Bonnet et al 1994, Squires et al 1996, Hoekstra et al 1998, Luppino & Kaiser 1997, Gray et al 2002). The 2-D shear field is also used to measure the large-scale structure distribution, and consequently to measure cosmological parameters (see e.g. van

Waerbeke et al 2001, Hoekstra 2002, Bacon et al 2002, Refregier et al 2002, Jarvis et al 2003, Brown et al 2003, Pen et al 2003).

Recently, there has been much interest in using redshift information with weak gravitational lensing in order to add depth to our picture of the mass distribution in the Universe. Lensing tomography has been developed as a means of studying the growth of the weak lensing power spectrum as a function of redshift (e.g. Seljak 1998, Hu 1999, 2002, Huterer 2002, King & Schneider 2002b), and the use of redshift information to remove the impact of intrinsic galaxy alignments on lensing measurements has been explored (Heymans & Heavens 2002, King & Schneider 2002a,b, Heymans et al 2003). Observationally, Wittman et al (2001, 2002) have used 3-D shear information to directly measure the mass and redshift of two clusters discovered through this shear field.

A further significant development has been the realisation that a full reconstruction of the 3-D gravitational potential and dark matter density field is possible using just weak shear and redshifts (Taylor 2001). A 3-D gravitational lensing analysis is clearly of importance for cosmology. With a 3-D analysis we will have, for the first time, a way of imaging the full dark matter distribution from cluster scales upwards and over a order of magnitude in redshift, independent of the galaxy distribution. With such depth one can hope to visually see the growth of structure. A 3-D lensing survey can also be used to construct a mass-selected galaxy cluster catalogue, which would have many important cosmological uses. A three dimensional lensing survey would remove the projection effects that contaminate standard 2-D projected surveys (White, van Waerbeke & Mackey, 2002). In the case of individual clusters this can cause biases in mass estimation due to both foreground and background structures. With a 3-D lensing analysis, both the mass and position of clusters can be found independently of the baryonic content.

Following Taylor (2001), Hu & Keeton (2003) subsequently developed a pixelised version of the 3-D reconstruction, while Bacon & Taylor (2003) examined the practical implementation of Taylor's (2001) method. Bacon & Taylor (2003) demonstrated that one can hope to reconstruct the gravitational potential on cluster mass scales with ground-based shear surveys to a depth of $z = 1$ by including photometric redshifts with accuracy $\Delta z \simeq 0.05$.

To date the idea of reconstructing the full 3-D gravitational or matter distribution has only been applied to simulated data. However, data of this quality already exist; the COMBO-17 survey (Wolf et al 2001) is a 17-band photometric redshift survey with accuracy $\Delta z = 0.05$ throughout $0 < z < 0.8$ and has already been used for weak shear studies of a supercluster (Gray et al 2002), large-scale structure (Brown et al 2002), star formation efficiency (Gray et al 2003) and galaxy alignment effects (Heymans et al 2003). It is therefore an ideal dataset with which to carry out a first direct reconstruction of the 3-D gravitational potential.

In this paper we carry out a full 3-dimensional analysis of the A901/2 supercluster field from the COMBO-17 survey, including measurements of the 3-D shear, lensing potential and gravitational potential fields. We describe the necessary methodological tools for these measurements in Section 2. In particular we summarise our approach to measurement of tangential shear, the Kaiser-Squires inversion

for the lensing potential and reconstruction of the gravitational potential. In Section 2 we also develop the halo model of mass and galaxy clustering allowing an analysis of the correlations between the 3-D gravitational potential and the galaxy number and luminosity densities. In Section 3 we describe the COMBO-17 dataset, discussing the imaging and photometric redshift data, and the means of obtaining a shear catalogue. We describe the A901/2 field in detail, recalling the relevant shear measurements obtained by Gray et al (2002) for this supercluster.

In Section 4 we measure the 3-D tangential shear of the COMBO-17 A901/2 supercluster field, where we fit 3-D shear models to the clusters, following the approach of Wittman et al (2001, 2002), and measure the mass and redshift for the clusters directly from the gravitational distortions. We examine the evidence for a lensing signature of a cluster behind the supercluster at $z = 0.48$, and constrain its mass using a two-cluster fit to the shear data. This is compared to the results of a 2-D lensing analysis by Gray et al (2002). In Section 5 we calculate the 3-dimensional lensing potential and reconstruct the 3-dimensional dark matter potential of the A901/2 supercluster field. We find significant potential wells at the expected position of the supercluster in 3-D, and also find a significant potential well at the position of the background cluster. We discuss the measurement significance for each of these detections.

In Section 6 we explore a natural application of 3-D gravity measurements to measure the auto- and cross-correlation of the 3-D gravitational potential with two other quantities: the galaxy number density, and the luminosity distribution. We find that there are anti-correlations for each of these quantities, and describe how this can be understood in terms of baryonic infall into dark matter concentrations. We compare our results with theoretical predictions of the halo model. Finally, we present our conclusions in Section 7.

2 METHODOLOGY

In this section we discuss the methodology we will use to extract 3-D information from our survey. We begin by discussing the tangential shear, which we will use for a χ^2 analysis of the mass and position of mass concentrations in our survey. Following this, we will describe our method for fully reconstructing the gravitational potential in 3-D. Finally we present and develop the halo model of nonlinear mass and galaxy clustering for analysing correlation functions of the gravitational potential, the galaxy number density and the galaxy luminosity fields.

2.1 Tangential shear

Weak gravitational shear distorts images in a way that can be described by the shear matrix

$$\gamma_{ij} = \begin{pmatrix} \gamma_1 & \gamma_2 \\ \gamma_2 & -\gamma_1 \end{pmatrix}, \quad (1)$$

where γ_1 and γ_2 represent the two orthogonal states of distortion (see e.g. Bartelmann & Schneider 2001). In Section 4 we use the methods discussed by Kaiser, Squires & Broadhurst (1995) to obtain γ_{ij} estimates for all galaxies in our survey, and use the tangential shear measurements to find

estimates of cluster mass and redshift position (c.f. Gray et al 2002). In order to do this, we choose a centre for each cluster, which we take to be the optical centre (see Section 4). We then calculate the tangential shear in radial bins around each cluster,

$$\gamma_t = -(\gamma_1 \cos 2\theta + \gamma_2 \sin 2\theta), \quad (2)$$

where θ is the position angle taken from the cluster centre. In order to estimate the mass and redshift of each cluster, we will fit a singular isothermal sphere to the tangential shear values (see Section 4).

2.2 Lensing Potential

To measure the 3-dimensional gravitational potential, we must first calculate the lensing potential, ϕ , which we consider as a 3-dimensional field (c.f. Taylor 2001, Bacon & Taylor 2003). This is related to the shear field (in the limit of a flat sky) by

$$\gamma_{ij}(r, \mathbf{r}\boldsymbol{\theta}) = \left(\partial_i \partial_j - \frac{1}{2} \delta_{ij}^K \partial^2 \right) \phi(r, \mathbf{r}\boldsymbol{\theta}), \quad (3)$$

where $\boldsymbol{\theta}$ is a position angle on the sky, $\partial_i \equiv r(\delta_{ij} - \theta_i \theta_j) \nabla_j = r(\nabla_i - \theta_i \partial_r)$ is the dimensionless transverse differential operator and $\partial^2 \equiv \partial_i \partial^i$ is the transverse Laplacian. Here r is a comoving distance,

$$r(z) = \int_0^z \frac{dz'}{H(z')}, \quad (4)$$

where

$$H(z) = H_0 [\Omega_m (1+z)^3 + \Omega_v]^{1/2} \quad (5)$$

is the Hubble parameter, Ω_m is the present-day matter density parameter and Ω_v is the energy density associated with the vacuum. Throughout we shall assume a spatially flat universe with $\Omega_m = 0.3$ and $\Omega_v = 0.7$.

The inverse relation, for calculating ϕ from γ_{ij} , is given by the Kaiser-Squires (1993) relation, generalised to 3-D:

$$\hat{\phi}(r, \mathbf{r}\boldsymbol{\theta}) = 2\partial^{-4} \partial_i \partial_j \gamma_{ij}(r, \mathbf{r}\boldsymbol{\theta}), \quad (6)$$

where $\hat{\phi}$ is an estimate of ϕ . In order to calculate this quantity in practice, the shear field must be smoothed in the transverse direction in order to overcome the formally infinite noise amplitude (Kaiser & Squires 1993). In this equation we have used the operator ∂^{-2} ; this is the (flat sky) inverse 2-D Laplacian operator, given by

$$\partial^{-2} \equiv \frac{1}{2\pi} \int d^2\theta \ln |\boldsymbol{\theta} - \boldsymbol{\theta}'|. \quad (7)$$

We measure transverse positions $\boldsymbol{\theta}$ in units of radians, leading to dimensionless lensing quantities.

Equation (6) reconstructs the lensing potential up to an arbitrary function of comoving distance (Taylor 2001, Bacon & Taylor 2003):

$$\hat{\phi}(r, \mathbf{r}\boldsymbol{\theta}) = \phi(r, \mathbf{r}\boldsymbol{\theta}) + \psi(r, \boldsymbol{\theta}), \quad (8)$$

where

$$\psi(r, \boldsymbol{\theta}) = \omega(r) + \eta(r)\theta_x + \mu(r)\theta_y + \nu(r)(\theta_x^2 + \theta_y^2), \quad (9)$$

and where $\omega(r)$, $\eta(r)$, $\mu(r)$ and $\nu(r)$ are arbitrary functions. Here ϕ is the true lensing potential, and $\psi(r, \boldsymbol{\theta})$ is a solution to

$$\left(\partial_i \partial_j - \frac{1}{2} \delta_{ij}^K \partial^2 \right) \psi(r, \boldsymbol{\theta}) = 0. \quad (10)$$

This arbitrary behaviour along the line-of-sight is due to the fact that the shear only defines the lensing potential up to a quadratic in angle for each slice in depth, and is the potential analogue of the more familiar sheet-mass degeneracy for the lens convergence, κ ; $\phi = 2\partial^{-2}\kappa + C$. These terms can be removed by taking moments of the measured lens potential over the area of a survey (Bacon & Taylor 2003);

$$\psi_{mn}(r) = \frac{1}{A} \int_A d^2\theta \hat{\phi}(r, \mathbf{r}\boldsymbol{\theta}) (\theta_x^m + \theta_y^n), \quad (11)$$

where A is the area of the survey. An estimate of the lensing potential with zero mean, gradient and paraboloid contributions is then given by

$$\Delta\phi(r, \mathbf{r}\boldsymbol{\theta}) = \hat{\phi}(r, \mathbf{r}\boldsymbol{\theta}) - \hat{\psi}(r, \mathbf{r}\boldsymbol{\theta}), \quad (12)$$

where $\hat{\psi}$ is a correction term composed of the coefficients ψ_{mn} . We have neglected higher order polynomial contributions to ϕ which could in general lead to a bias in the estimated gradient and paraboloid terms; however, in practice our boundary conditions at the field edge (continuity for amplitude and gradient) mean that we do not have such terms in our reconstruction.

For a general survey geometry, the coefficients ψ_{mn} can be calculated numerically. The removal of the first few moments will reduce the power on the largest scales of the survey. This effect and the noise properties of the reconstructed $\Delta\phi$ field are discussed further in Bacon & Taylor (2003).

2.3 Gravitational Potential

Having calculated an estimate of the lensing potential, $\Delta\phi$, we are now in a position to reconstruct the 3-D gravitational potential. The lensing potential is related to the gravitational potential by the line-of-sight integral

$$\phi(r, \mathbf{r}\boldsymbol{\theta}) = 2 \int_0^r dr' \left(\frac{r-r'}{rr'} \right) \Phi(r', r'\boldsymbol{\theta}), \quad (13)$$

where we have assumed a spatially flat universe and the Born approximation. Treating $\phi(r, \mathbf{r}\boldsymbol{\theta})$ as a 3-D variable, we can invert equation (13) to arrive at an estimate of the 3-D gravitational potential (Taylor 2001):

$$\Phi(r, \mathbf{r}\boldsymbol{\theta}) = \frac{1}{2} \partial_r r^2 \partial_r \phi(r, \mathbf{r}\boldsymbol{\theta}), \quad (14)$$

where $\partial_r = \boldsymbol{\theta} \cdot \nabla$ is a radial derivative. The solution to equation (14) can be checked by direct substitution into equation (13) and integrating by parts. In practice we shall use the corrected potential, $\Delta\phi$, from equation (12), yielding

$$\Phi(r, \mathbf{r}\boldsymbol{\theta}) = \frac{1}{2} \partial_r r^2 \partial_r \Delta\phi(r, \mathbf{r}\boldsymbol{\theta}) \quad (15)$$

as an estimate of the dark matter potential. For completeness we note that the density field is

$$\delta(r, \mathbf{r}\boldsymbol{\theta}) = \frac{a(r)}{3\Omega_m H_0^2} \nabla^2 \partial_r r^2 \partial_r \Delta\phi(r, \mathbf{r}\boldsymbol{\theta}), \quad (16)$$

where a is the expansion factor. However the dataset we shall consider here is too noisy to reconstruct the 3-D density field. Hence we shall use the set of equations, (6), (11), (12) and (15) to generate the 3-D lensing convergence, 3-D

lensing potential and 3-D dark matter potential from combined shear and redshift information.

2.4 Wiener filtering

Hu & Keeton (2003) and Bacon & Taylor (2003) have shown that reconstruction of the 3-D gravitational potential benefits enormously from Wiener filtering. For realistic lensing surveys cluster-mass concentrations are typically undetectable in the unfiltered gravitational potential, due to the large shot-noise. However cluster masses can be detected with a signal-to-noise ratio of $\simeq 2$ *per pixel* in the Wiener filtered field. We need only filter in the redshift direction (Bacon & Taylor, 2003), leaving the potential field in the transverse direction unfiltered.

For each x, y position, we construct a vector, Φ_i , composed of the gravitational potential measurement in the i^{th} redshift bin, along the z direction. We also construct a noise covariance matrix, N_{ij} , for the gravitational potential covariance in the z direction, measured from 100 reconstructions of the Φ -field with randomised ellipticities. A further matrix, S_{ij} , represents the expected signal covariance along the line of sight. For this we use a unit matrix multiplied by $S = (1.3 \times 10^{-7})^2$ which equals the square of the expected gravitational potential amplitude for a $5 \times 10^{13} M_\odot$ cluster (c.f. Bacon & Taylor 2003);

$$S_{ij} = S\delta_{ij}. \quad (17)$$

We then apply the Wiener filtering,

$$\Phi' = S(S + N)^{-1}\Phi, \quad (18)$$

where Φ' is the Wiener filtered gravitational potential we require.

2.5 Statistical properties and the halo model

Having shown how one can reconstruct the 3-D Newtonian gravitational potential from lensing, we now turn to the statistical properties of the reconstructed field. In addition to the gravitational field, we can also measure the 3-D galaxy number density, $n(\mathbf{r})$, and the luminosity density, $L(\mathbf{r}) \equiv \rho_L(\mathbf{r})$. It is of interest to estimate the auto- and cross-correlations of these fields from theory, in order to compare with the results of our data analysis.

In practice we shall use a projected correlation function, where the statistical correlations are calculated in slices in redshift and then averaged. This is convenient since each redshift bin is much larger than the transverse size of the field, and helps to reduce the effect of the line-of-sight Wiener filter which will distort the statistical properties of the filtered field. We define the projected correlation between two fields, X and Y , by

$$C^{XY}(r_\perp) = \frac{1}{N_z} \sum_{i=1}^{N_z} \langle X(\mathbf{x}_\perp, z_i) Y(\mathbf{x}_\perp + \mathbf{r}_\perp, z_i) \rangle, \quad (19)$$

where X and Y denote the fields (Φ, n, L), \mathbf{x}_\perp and \mathbf{r}_\perp are transverse position vectors in the slice at redshift z_i , and $r_\perp = |\mathbf{r}_\perp|$. The number of redshift slices is N_z . The averaging, $\langle \dots \rangle$, is taken over the fields at each slice. In practice this averaging will be done over a finite survey on the sky with pixelised data.

The observed Φ - Φ , Φ - n and Φ - L projected auto- and cross-correlation functions can be generated from their corresponding power spectra by the transformation

$$C^{XY}(r_\perp) = \int \frac{k^2 dk}{2\pi^2} W(k, r_\perp) P_{XY}(k) |\omega_{\text{pix}}(k)|^2, \quad (20)$$

where for a cylindrical survey with radius $R_s = 4 h^{-1} \text{Mpc}$ and length $L_s = 1000 h^{-1} \text{Mpc}$ the survey window function is given by

$$W(k, r_\perp) = \int_{-1}^1 d\mu j_0^2(k L_{\text{pix}} \mu) [1 - W_o^2(k R_s \sqrt{1 - \mu^2})] \times [J_0(k r_\perp \sqrt{1 - \mu^2}) - W_o(k R_s \sqrt{1 - \mu^2})] \quad (21)$$

where

$$W_o(x) = \frac{2J_1(x)}{x}, \quad (22)$$

is the 2-D Fourier transform of a circular survey aperture. $L_{\text{pix}} = 50 h^{-1} \text{Mpc}$ is the pixel length in the redshift direction. We also include the effects of pixelisation in the transverse direction with the pixel window function;

$$\omega_{\text{pix}}(k) = \int_{-1}^{+1} d\mu W_o(k R_{\text{pix}} \sqrt{1 - \mu^2}), \quad (23)$$

for circular pixels of radius $R_{\text{pix}} = 0.2 h^{-1} \text{Mpc}$. The various terms in equation (21) then correct for pixelisation, the survey window function, and removal of the mean field. There is also an integral constraint, that the integral of the field is zero when averaged over the survey volume.

The statistical properties of dark matter and galaxies can be most easily modeled theoretically with the halo model (e.g. Peacock & Smith 2000, Seljak 2000). Here the statistical distribution of dark matter is considered as a sum of linear correlations between haloes on large scales and internal correlations within haloes on small scales. These haloes can be populated with a distribution of galaxies and allocated a luminosity, depending on the halo mass. The statistical properties of the haloes and galaxies can then be calculated by averaging over the mass function. The power spectra we require is given by a linear and a nonlinear term;

$$P_{XY}(k) = \int \frac{dn(M)}{(2\pi)^3} \left(\frac{\rho(k, M)}{\bar{\rho}} \right)^2 W_{XY}(k, M) + P_{XY}^{\text{LIN}}(k), \quad (24)$$

where $dn(M) = dM(dn/dM) = (\bar{\rho}/M)f(\nu)d\nu$ and $f(\nu)$ is the Tolman-Sheth mass function,

$$\nu f(\nu) = A \left(1 + \left(\frac{\nu}{\sqrt{2}} \right)^{-0.3} \right) \left(\frac{\nu}{\sqrt{2}} \right)^{1/2} e^{-\nu/2\sqrt{2}}, \quad (25)$$

where $\nu(M, z) = (\delta_c(z)/\sigma(M, z))^2$ and $\sigma^2(M, z)$ is the variance on the scale of haloes of mass m at redshift z . We use a critical collapse overdensity of $\delta_c = 1.68/(1+z)$. The halo profile, $\rho(r, M)$, is assumed to be a Navarro-Frenk-White (NFW; 2000) profile;

$$\rho(r, M) \propto \frac{1}{(r/r_s)^{-\alpha}(1+r/r_s)^{3+\alpha}}, \quad (26)$$

where the inner slope is $\alpha = -1$, the inner core radius is $r_s = r_v/c$, where $r_v = 3M/(4\pi\bar{\rho}\delta_{\text{vir}})$ is the virial radius and $c = 10(M/M_*)^\beta$ is a halo concentration factor. We assume $M_* = 8 \times 10^{11} h^{-1} \text{M}_\odot$ (Guzik & Seljak 2002) and

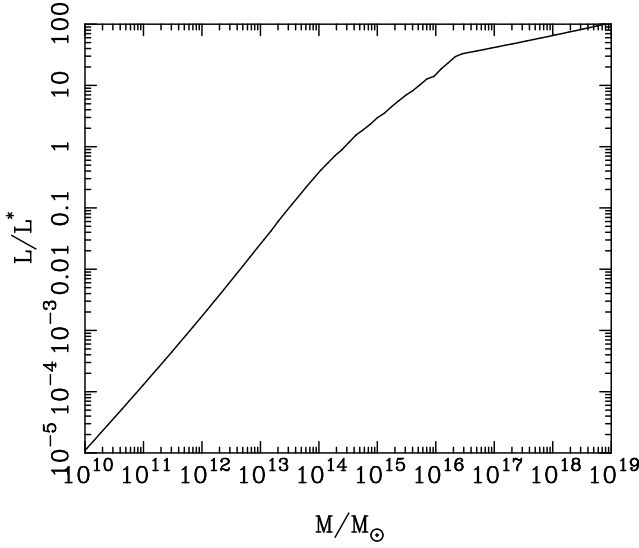


Figure 1. The luminosity-mass relation, $L(M)$, for the COMBO-17 data set, estimated from equating the cumulative R-band luminosity and Tolman-Sheth mass functions.

$\beta = -0.2$. The Fourier transform of the NFW halo profile with a sharp cut-off at the virial radius is given by

$$\rho(k, M) = k \cos(k) [\text{Ci}(k(1+c)) - \text{Ci}(k)] + k \sin(k) [\text{Si}(k(1+c)) - \text{Si}(k)] - \frac{\sin ck}{1+c}, \quad (27)$$

where $\text{Ci}(z)$ and $\text{Si}(z)$ are the Cosine and Sine integrals, respectively. For simplicity we shall assume that the linear power spectrum of all of the fields is just equal to the linear dark matter power spectrum.

The weighting functions in the nonlinear, halo-halo part of equation (24) are given by

$$W_{\Phi\Phi}(k, M) = \frac{9}{4} H_0^4 \Omega_m^2 (1+z)^2 k^{-4} \quad (28)$$

for the potential power spectrum, and

$$W_{nn}(M) = \frac{\langle N(N-1) \rangle \bar{\rho}^2}{(\bar{n}M)^2} \quad (29)$$

for the galaxy-galaxy power spectrum, where $\langle N(N-1)(M) \rangle$ is the variance of the number of galaxies in a halo of mass M . The galaxy-mass weight is given by

$$W_{n\Phi}(k, M) = -\frac{3}{2} H_0^2 \Omega_m (1+z) k^{-2} \frac{\langle N \rangle \bar{\rho}}{\bar{n}M}, \quad (30)$$

where $\langle N(M) \rangle$ is the average number of galaxies for a halo of mass M . We model the halo occupation numbers with the same functional form;

$$\langle N \rangle, \langle N(N-1) \rangle^{1/2} = \left(\frac{M}{M_*} \right)^{0.81} \left(1 - e^{-(M/M_0)^2/2} \right), \quad (31)$$

where $M_* = 10^{13.47} M_\odot$. For the mean occupation number, $\langle N \rangle$, we use $M_0 = 10^{13} M_\odot$, while for the scatter in the occupation number, $\langle N(N-1) \rangle$, we use $M_0 = 6 \times 10^{12} M_\odot$. These parameters are suitable for all galaxies with an absolute magnitude threshold of $M_B < -19.5$ (eg Seljak 2000).

The luminosity-mass weight is given by

$$W_{L\Phi}(k, M) = -\frac{3}{2} H_0^2 \Omega_m (1+z) k^{-2} \left\langle \frac{M}{L} \right\rangle \frac{L(M)}{M}, \quad (32)$$

where $\langle M/L \rangle$ is the universal mass-to-light ratio and $L(M)$ is the average luminosity of a halo of mass M . Finally the luminosity-luminosity weight is

$$W_{LL}(M) = \left\langle \frac{M}{L} \right\rangle^2 \left(\frac{L(M)}{M} \right)^2. \quad (33)$$

The luminosity-mass relation, $L(M)$, can be estimated by equating the cumulative halo number density to the cumulative luminosity function, $N(> M) = N(> L)$ (Peacock & Smith 2000). We use the R-band luminosity function derived by Wolf et al (2003) for the COMBO-17 data. Figure 1 shows the derived luminosity-mass relation for the COMBO-17 dataset.

We should also consider the range of the mass integration in equation (24). In a finite survey, the high-mass end of the mass function may not be well sampled, as high mass concentrations are rare. To account for this, and to compare results with a real survey, we may truncate this integral at the largest mass found in the survey. This will have the effect of suppressing the largest nonlinear scales. As the potential field is weighted towards larger scales, this can have an important effect on the statistics of the potential field. We discuss this further in Section 6.

Having presented our methods for recovering the 3-D dark matter gravitational potential field, and the halo model for analysing the auto- and cross-correlation of the gravitational potential, number density and luminosity densities, we now turn to the dataset we will apply this analysis to.

3 THE COMBO-17 DATA

3.1 Observations

The quality of data required for a full 3-D gravitational lensing analysis already exists. The COMBO-17 survey is a 17-band photometric redshift survey with gravitational lensing quality R-band data (Wolf et al 2001). The survey consists of four separate areas, each of $30' \times 30'$ comprising a total of 1 square degrees. All of the fields were observed using the Wide-Field Imager (WFI) at the MPG/ESO 2.2m telescope on La Silla in Chile, with a 4×2 array of 2048×4096 pixel CCDs, each pixel subtending 0.238 arcseconds. One of these fields is centred on the A901/2 supercluster which has previously been analysed by Gray et al (2002) and it is this field that we will use in this analysis.

3.1.1 Photometric redshifts

Each of the COMBO-17 fields was observed in 17 different filters, with the intention of obtaining object classification and accurate photometric redshifts. In order to provide reliable redshifts, the filter set included five broad-band filters (*UBVRI*) and 12 medium-band filters from 350 to 930 nm. This observing strategy allows simultaneous estimates of Spectral Energy Distribution (SED) classifications and photometric redshifts from empirically-based templates. Wolf et al (2001) describe in detail the photometric redshift estimation methods used to obtain typical accuracies of $\sigma_z = 0.05$ for galaxies throughout $0 < z < 1$.

3.1.2 Shear measurements

The R filter was used in best seeing conditions throughout the observing campaign, in order to provide a deep R -band image from which to measure the gravitational shear. Gray et al (2002) discuss the procedure used to reduce the R band imaging data, which totalled 6.3 hours. As described there, the 352 individual chip exposures for the A901/2 field were registered using linear astrometric fits, with 3σ bad pixel rejection to remove bad columns and pixels.

We then applied the *imcat* shear analysis package, using Kaiser, Squires & Broadhurst's (1995) weak lensing measurement method, to our reduced image (see Gray et al 2002 for details). This resulted in a catalogue of galaxies with centroids and shear estimates throughout our field, corrected for the effects of PSF circularisation and anisotropic smearing. We appended to this catalogue the photometric redshifts estimated for each galaxy from the standard COMBO-17 analysis of the full multicolour dataset. Of the 37,243 galaxies in the shear catalogue, 36% had a reliable photometric redshift, the remainder being fainter than the $R = 24$ reliability limit of the redshift survey. The requirement for the 3-D lensing study that the redshift of each galaxy be known clearly results in an immediate reduction in available galaxies, as it is apparent that most of the background sample is composed of galaxies that are small and fainter than the magnitude limit of the redshift survey.

3.2 The A901/2 supercluster

The supercluster itself is composed of three clusters of galaxies (A901a, A901b, and A902), all at $z = 0.16$ and contained within the $0.5^\circ \times 0.5^\circ$ field-of-view of the WFI. The X-ray, number count, and 2-dimensional lensing properties of the field are discussed in detail in Gray et al (2002). Figure 2 shows the projected mass distribution estimated by Gray et al (2002). The three main components of the supercluster, A901a, A901b and A902 are clearly detected. One of the main conclusions of that work was that the distribution of the early-type supercluster galaxies (as selected by their location on the $B - R$ vs R colour-magnitude diagram) does not fully trace the distribution of the lensing-revealed mass map. In particular, misalignments between (early-type) light and mass were found in A901b which is the only cluster to display extended X-ray emission in pointed ROSAT HRI observations by Schindler (2000).

Additionally, no single mass-to-light ratio (again, considering only the light from the colour-selected early-type galaxies) could be adequately determined for the system as a whole: A901a, by far the most luminous of the clusters, was under-represented in the lensing mass map. Clearly, the mapping from early-type light to mass in this system is not a linear one, either due to dynamical effects from an ongoing merger or to divergent paths in galaxy evolution (and hence total luminosity) in the three clusters.

The Gray et al. (2002) lensing study employed a standard weak lensing approximation and assumed that all the mass measured in the projected mass map was due to a mass concentration in a single lens plane. However, with the advent of 3-dimensional mapping techniques, we are now able to fully probe the mass distribution throughout the entire volume of the COMBO-17 observations. This advance al-

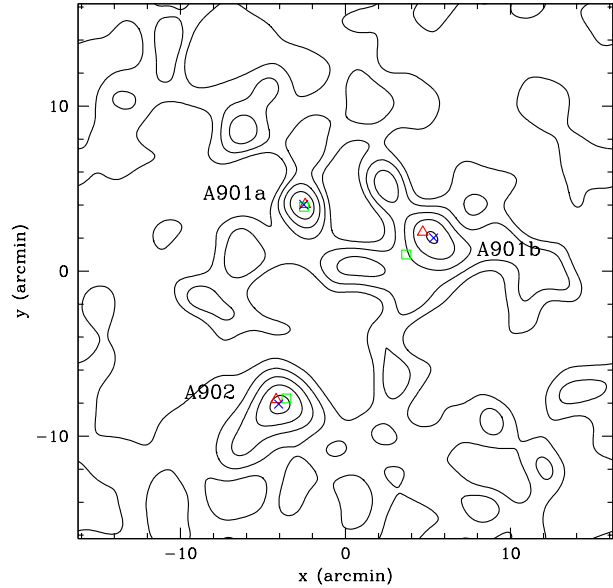


Figure 2. Two-dimensional projected distribution of mass in the A901/2 field. The contours show the lensing mass map of Gray et al. (2002), with crosses, squares, and triangles marking the location of the peaks in the mass and light distributions and the positions of the brightest cluster galaxies, respectively. The contour levels are spaced by $\Delta\kappa = 0.02$, while the noise level is $\sigma_\kappa = 0.027$.

lows us to test whether the bulk of the mass does indeed lie in the redshift plane of the supercluster at $z = 0.16$, or whether projection effects from matter behind the supercluster contribute significantly. If projection effects are found to contribute significantly to the 2-dimensional mass map, we may have an alternative explanation to discrepant M/L ratios observed in the system.

4 MEASURING THE MASS AND 3-D POSITION OF CLUSTERS

4.1 Single cluster model

Using the shear estimates for the galaxies in the A901/2 field, together with photometric redshifts, we are able to measure the redshifts and masses of the clusters from the 3-D distortion field that they create. While constraining cluster masses has been the traditional goal for weak lensing studies, it is also of importance to be able to place additional constraints on the mass distribution along the line of sight using a method that is independent of baryonic content. While in this case the structures we are probing are clear overdensities of galaxies at known redshift, we shall use this supercluster field as an illustration of what can be achieved when the shear signal from each lensed galaxy can be appropriately weighted by its redshift. One possible application of such a technique would be as a way to confirm and constrain the masses and redshift of ‘dark clusters’ (Erben et al. 2000, Gray et al. 2001, Umetsu & Futamase 2003, Weinberg & Kamionkowski 2003), or to deproject multiple mass concentrations along a single line-of-sight. In addition,

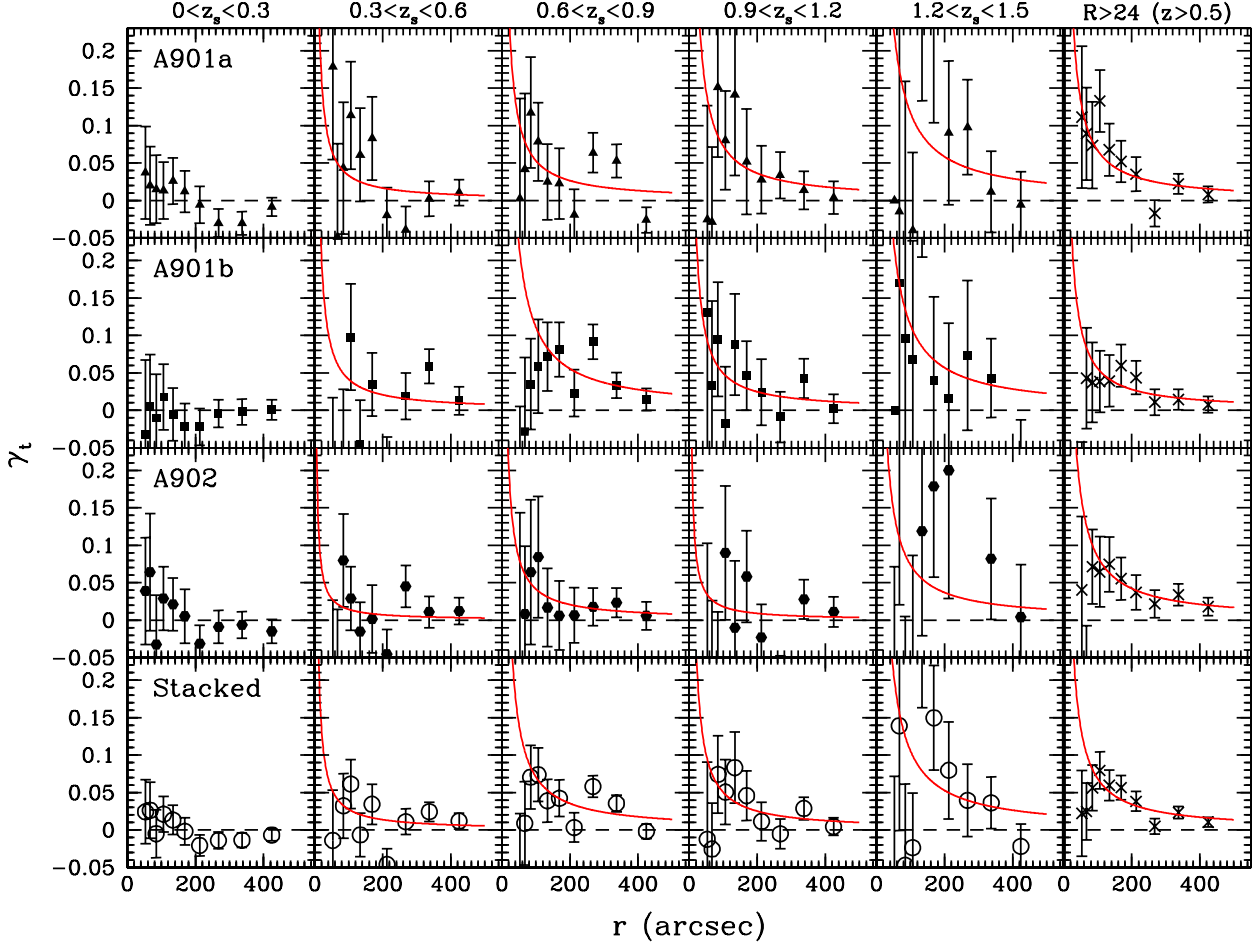


Figure 3. Tangential shear as a function of angular radius and redshift. Each row presents the radial profile of the tangential shear around each of the three mass peaks in the field, according to increasing source redshift. The solid curve in each case represents with best-fit SIS model for the redshift bin, with $z_{\text{lens}}=0.16$. Note the growth of the lensing signal as the slices in redshift space become more distant. The bottom row shows the signal for an ‘average’ cluster, calculated by stacking the catalogues for the three clusters around a common origin (no attempt is made to scale the signal according to varying cluster mass).

3-D lensing offers the possibility of creating mass-selected samples of dark matter concentrations. Such a sample would allow for cleaner comparisons with theories of structure formation, without resorting to a priori assumptions about how the dark matter and baryonic distribution (in the form of galaxies or hot X-ray gas) are related.

Consequently, in the following analysis we will treat the masses and (known) redshifts of each cluster as free parameters. Figure 3 shows the radial profile of the tangential shear, $\gamma_t(\theta)$ (Equation 2), as a function of source redshift for each cluster, z_s . In this figure each row represents a different cluster, with the final row representing the results from a ‘stacked’ cluster, obtained by recentering all three catalogues about a common origin and concatenating. Each column shows the shear signal in increasing source redshift slices. The solid curves show the best-fit tangential shear for a singular isothermal sphere (SIS) model;

$$\gamma_{t,\text{SIS}}(\theta) = \frac{2\pi}{\theta} \left(\frac{\sigma_v}{c} \right)^2 \frac{D_{ls}}{D_s}. \quad (34)$$

Here D_{ls} and D_s are the angular distances from lens to

source and from observer to source, respectively. We fix the lens redshift at $z_{\text{lens}} = 0.16$ so that the SIS model is characterized only by a single parameter, the halo velocity dispersion, σ_v . The final column in Figure 3 shows the shear profile for the $\sim 65\%$ of source galaxies with $R > 24$, for which photometric redshifts are unreliable. As expected, the lensing signal generally grows as a function of source redshift behind each cluster, and no signal is detected in the lowest redshift ($0 < z_s < 0.3$) bin where many of the source galaxies are foreground to the lens.

Figure 4 shows the constraints on mass and redshift for the clusters from a 2-parameter χ^2 fit of the data points from Figure 3, allowing both z_{lens} and σ_v to vary. For A901a the best-fit z_{lens} is $z_{\text{lens}} = 0.30^{+0.10}_{-0.16}$ and a small range in preferred mass of $\sigma_v = 840^{+100}_{-105} \text{ km s}^{-1}$. For A901b, we obtain $z_{\text{lens}} = 0.38^{+0.14}_{-0.11}$ and $\sigma_v = 840^{+170}_{-110} \text{ km s}^{-1}$. For A902 the best-fit parameters are $z_{\text{lens}} = 0.38^{+0.23}_{-0.20}$ and $\sigma_v = 760^{+220}_{-200} \text{ km s}^{-1}$. As expected, the increased number density in the ‘stacked’ catalogue results in slightly smaller error bars: $z_{\text{lens}} = 0.38^{+0.05}_{-0.09}$ and $\sigma_v = 840^{+25}_{-100} \text{ km s}^{-1}$. In each case the degeneracy in the contours is clear and the

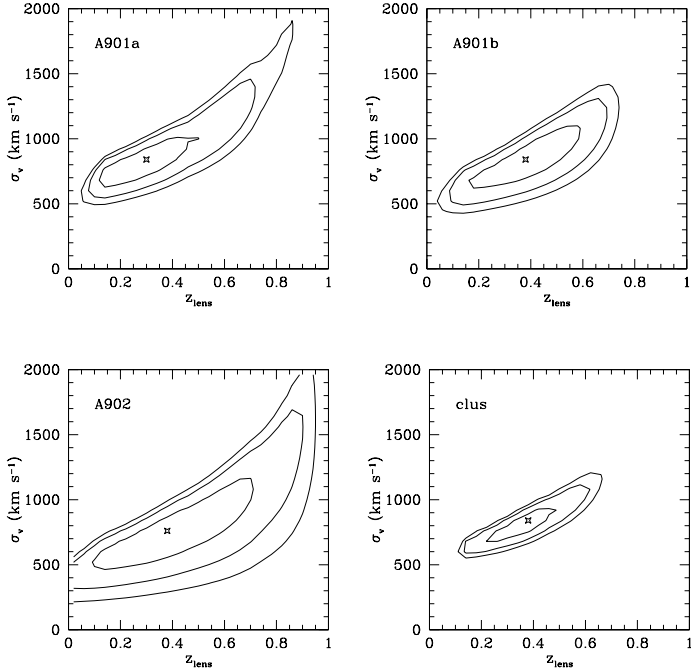


Figure 4. Constraints on cluster mass and redshift. Each panel shows the 1, 2 and 3-sigma (68%, 95% and 99.5% confidence) contours for a χ^2 two-parameter fit to the data from Figure 1, allowing both z_{lens} and σ_v (for a SIS model) to vary for each cluster.

best-fit redshift is biased towards higher redshifts, although in no case is the true solution of $z_{\text{lens}} = 0.16$ excluded at the 95% confidence level. This is partially the result of the coarseness of the redshift bins: much of the signal constraining the redshift of the cluster comes from the rapid rise in lensing signal just beyond the lens redshift. In this case our lowest-redshift bin spans the relatively wide redshift slice of $0 < z_s < 0.3$. A finer redshift slice would remove some of this degeneracy, for example if $\Delta z = 0.1$ the best-fit solution for the redshift of A901a falls to $z_{\text{lens}} = 0.22$. However, a balance needs to be struck between ensuring fine adequate sampling in redshift space and having sufficient numbers of galaxies in each redshift bin.

Note that in each case, there is a strong detection of the clusters; the χ^2 results are not consistent with zero mass. This provides us with estimates of the detection significance of the clusters by marginalising over redshift, and examining how likely zero mass is in the resulting probability contours. For A901a, we find that the probability of a zero-mass solution at $z_{\text{lens}} = 0.16$ is 4.7×10^{-8} ; for A901b, 8×10^{-6} ; and for A902, 9×10^{-3} . Thus all clusters are highly significant mass concentrations.

If we fix the redshift of the clusters at $z = 0.16$ and fit only the velocity dispersions, then the best-fit results are: A901a, $\sigma_v = 680^{+25}_{-90} \text{ km s}^{-1}$; A901b, $\sigma_v = 600^{+40}_{-85} \text{ km s}^{-1}$; and A902, $\sigma_v = 520^{+55}_{-90} \text{ km s}^{-1}$. These values are our best estimates for a single cluster model and are tabulated in Table 1, along with the implied total mass within a $0.5 h^{-1} \text{ Mpc}$ radius. These results can be compared with those of Gray et al (2002) who measured the tangential shear for the faint $R > 22$ galaxies without any redshift information. They found

the velocity dispersion of $\sigma_v = 542^{+195}_{-333} \text{ km s}^{-1}$ for A901a, $\sigma_v = 659^{+129}_{-161} \text{ km s}^{-1}$ for A901b and $\sigma_v = 738^{+244}_{-384} \text{ km s}^{-1}$ for A902. All of these are in consistent within the errors with our current measurements for a similar fixed redshift of $z = 0.16$.

Figure 5 shows the tangential shear, $\gamma_t(\theta)$, as a function of redshift in the direction of each cluster, and for the ‘average’ stacked cluster. The shear data points in this plot, and their uncertainties, are from the fit of the SIS model to the data in Figure 3 in each redshift bin, and plotted at the centre of each bin. As a demonstration of the growth of the signal, we choose to plot the amplitude of these fits at the fiducial radius of $\theta = 200''$, although we emphasize that the fit is to *all* of the data points in Figure 3. We show the amplitude of the fit for each of the redshift bins, and for the $R > 24$ sample with unknown redshifts. In each figure we also show the best-fit shear model with parameters given by Figure 4 (dotted line) and a model with fixed cluster redshift of $z = 0.16$ and a shear amplitude normalised to the $R > 24$ galaxies at $z = 1$ (solid line; note that any similar normalisation at $z > 1$ would yield similar results).

The amplitude of the tangential shear as a function of redshift for A901a, shown in Figure 5 (top left), is in good agreement with the predicted shear for a $z = 0.16$ cluster with velocity dispersion given by Figure 4 (dotted line). In particular the A901a data shows a clear rise in the tangential shear signal from zero at the cluster redshift. There is also good asymptotic agreement with the $R > 24$ galaxies. A901b and A902 (Figure 5, top right and bottom left) both show similar trends of increasing shear, although in the case of A901b with a high shear signal in the $z_s = 0.75$ bin. This can be seen in the higher fit of the model to the data in Figure 2 in the redshift range $0.6 < z < 0.9$, and is mainly due to a high shear at $\theta > 200''$.

Finally, in addition to determining the lens strength and redshift, Figure 5 shows that the converse can also be achieved: by comparing the shear signal in the $R > 24$ bin (which contains $\sim 65\%$ of the galaxies in our shear catalogue) with either those of known redshift or the tangential shear of the best-fit model of the stacked clusters, the redshift of the $R > 24$ sources can be constrained to be $z_s > 0.5$ at the 1- σ level. As many lensing studies suffer significant errors resulting from the unknown redshift of the background sources, this result illustrates the potential for calibrating the redshifts of galaxies beyond the limit of both spectroscopic and photometric redshift surveys (see also Clowe et al 2003). The example given here is rather weak, as all of the major clusters are at a single redshift, $z = 0.16$ and the shear signal reaches asymptotic values relatively quickly. Ideally one would like to perform such an analysis with clusters at a range of redshifts, preferably at higher redshift to better constrain the unknown population.

4.2 A two cluster model along the line of sight

In the previous section we have demonstrated the constraints that the shear data together with the COMBO-17 photometric redshifts can place on the mass and redshift of a cluster, assuming that all the deflecting mass is located in a single plane. However, the redshift survey indicates that the galaxy distribution in the volume of observation in this field is not dominated simply by the $z = 0.16$ superclus-

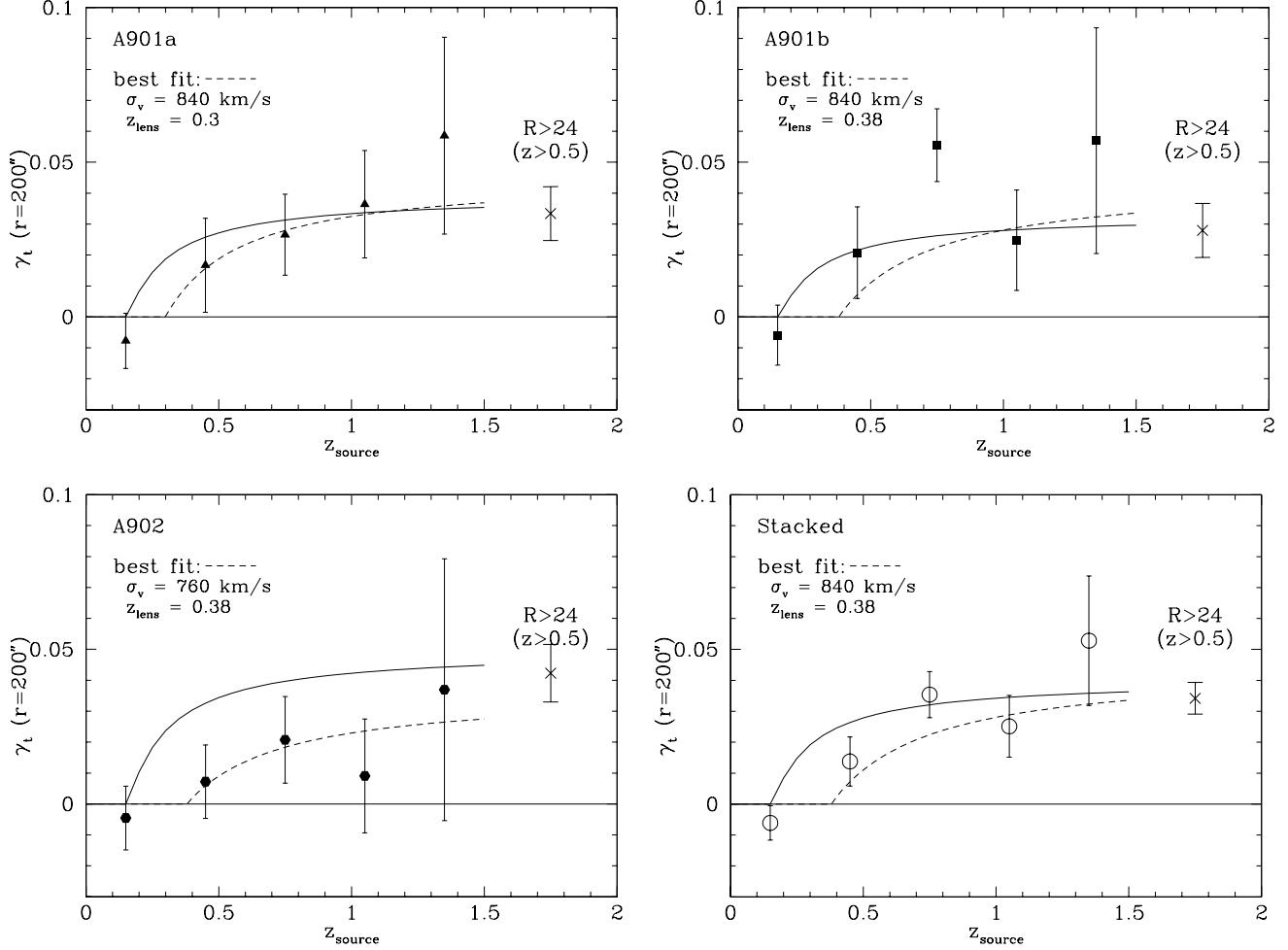


Figure 5. Tangential shear as a function of redshift. Each point represents the amplitude of the tangential shear from the fit to the SIS radial profile in each redshift slice from Fig. 3, plotted at a fiducial radius of 200 arcsec. The dashed line shows the expected redshift dependence from the best two-parameter fit ($z_{\text{lens}}, \sigma_v$) shown in Fig. 4. The solid curve shows the redshift dependence for a cluster at fixed redshift, with $z_{\text{lens}} = 0.16$, and with the amplitude normalised at $z = 1$ to the $R > 24$ point.

ter structure. In particular, we find that the photometric redshift survey reveals a second cluster, which we will term CB1, at higher redshift ($z = 0.48$) and located only ~ 90 arcsec to the southeast of the brightest cluster galaxy in A902. In this section we shall exploit this fortuitous alignment of two clusters and extend our analysis to fit a more complex mass model along the line of sight. This provides us with the opportunity to attempt to detect two co-projected clusters via their gravitational shear (c.f. Bacon & Taylor 2003, Hu & Keeton 2003), and measure their redshifts and velocity dispersions. In Section 5 we will show that this model is consistent with the Wiener filtered gravitational potential map which we will obtain which also shows a cluster-sized mass concentration at this redshift.

We perform a χ^2 fit for two colinear SIS profiles in a four-dimensional space of $\chi^2(z_1, \sigma_{v,1}, z_2, \sigma_{v,2})$, for two cluster velocity dispersions and redshifts, to the shear pattern and photometric redshifts behind the cluster A902, using the methods outlined above. The cluster redshifts are constrained so that $z_2 > z_1$. We find that the global minimum in this four-parameter space is located at $z_1 = 0.21$,

$\sigma_{v,1} = 350 \text{ km s}^{-1}$ and $z_2 = 0.45$, $\sigma_{v,2} = 650 \text{ km s}^{-1}$. By way of comparison, when we apply the same approach to A901a and A901b the first cluster solution in each case is consistent with the single-cluster model of the previous section, while the second cluster solution is pushed to the highest redshift and highest mass end of the four-parameter space.

Figures 6, 7 and 8 show marginalised projections of the full four-parameter space for the A902/CB1 clusters. Figure 6 shows the 68%, 95% and 99.5% confidence regions for $\chi^2(z_1, z_2)$, after marginalising over $\sigma_{v,1}$ and $\sigma_{v,2}$. Since we require $z_2 > z_1$ the lower triangle is excluded. The peak value for the lower redshift cluster is at $z_1 = 0.4$. The higher redshift cluster is best fit at $z_2 > 1.1$, but with a secondary minimum visible at $z \sim 0.5$. The reason for this can be seen in the tangential shear as a function of redshift for A902 in Figure 5. The shear amplitude low in the second bin at $z = 0.5$, so that the fit pushes the low cluster to slightly higher redshift than its true value at $z = 0.16$. The low shear in the $z = 1$ bin also means there is a jump in shear values in higher redshift bins, causing the fit to infer the second cluster is most likely here.

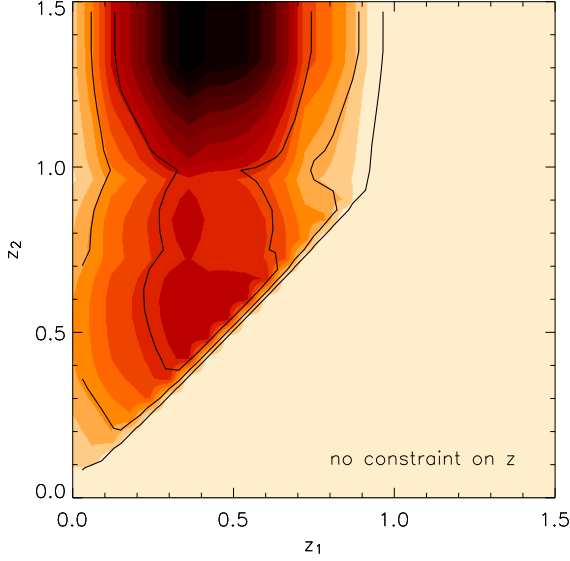


Figure 6. Contours of 68%, 95%, and 99.5% confidence constraints on the marginalised $\chi^2(z_1, z_2)$ distribution for a two-cluster model along line of sight through A902 centre. Here we have marginalised over $\sigma_{v,1}$ and $\sigma_{v,2}$ with $z_1 < z_2$.

Figure 7 shows the distribution for $\chi^2(\sigma_{v,1}, \sigma_{v,2})$ after marginalizing over redshifts, (z_1, z_2) . Here we have included a weak prior requiring that $z_1 < z_2 < 1$ to restrict the parameter space to more reasonable values. The results, with 68% confidence limits, are $\sigma_{v,1} = 550^{+200}_{-300} \text{ km s}^{-1}$ and $\sigma_{v,2} = 670^{+200}_{-550} \text{ km s}^{-1}$. If we drop this weak prior we find that $\sigma_{v,1} = 650^{+300}_{-200} \text{ km s}^{-1}$, while the second cluster velocity dispersion is unconstrained within the parameter space.

Finally, we can use our knowledge of the exact positions of A902 and CB1, in this case from the peaks in the 3-D galaxy number density distribution, to further improve our estimates of the two masses. We shall refer to this as a strong prior on the cluster positions, where we perform a χ^2 fit to two cluster velocity dispersions with fixed redshifts at $z_1 = 0.16$ and $z_2 = 0.48$.

Fig. 8 (top) shows the results for this fit. The formal minimum lies at a solution with $\sigma_{v,1} = 350 \text{ km s}^{-1}$ and $\sigma_{v,2} = 670 \text{ km s}^{-1}$. The total mass of the two-cluster system is well-constrained, although again the individual velocity dispersions are not. However, marginalising over each velocity dispersion separately (Fig. 8, bottom panel) we find the projected 1-parameter minimum χ^2 values are $\sigma_{v,1} = 470^{+100}_{-280} \text{ km s}^{-1}$ and $\sigma_{v,2} = 730^{+160}_{-340} \text{ km s}^{-1}$. These are then our best estimates of the masses of A902 and CB1, and are tabulated in Table 1. This demonstrates that we are able to measure the masses of two clusters along the same line of sight using shear and redshift data alone.

Interestingly, even with zero mass in the second cluster ($\sigma_{v,2} = 0 \text{ km s}^{-1}$), putting all of the mass in the first cluster, the most likely value for the velocity dispersion of the first cluster is $\sigma_{v,1} = 570 \pm 120 \text{ km s}^{-1}$. This is slightly lower than the result of Gray et al (2002) for A902 of $\sigma_v = 738^{+244}_{-384} \text{ km s}^{-1}$, although there is a good overlap with the uncertainties. One possible reason for the change in the single cluster velocity dispersion of A902, with fixed redshift,

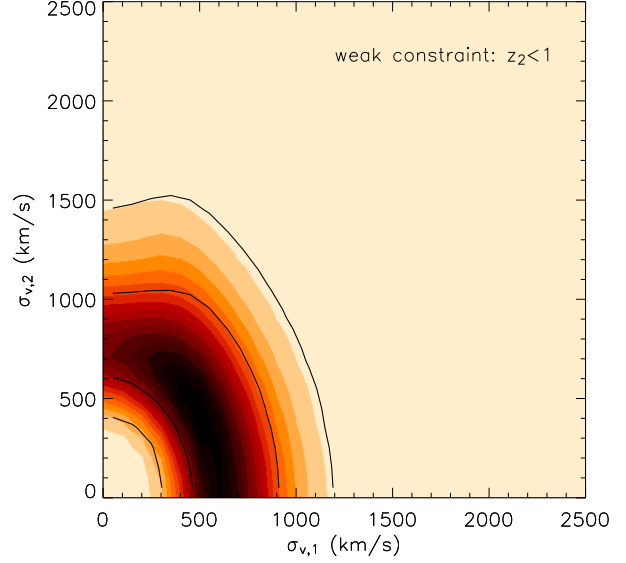


Figure 7. Contours of 68%, 95%, and 99.5% confidence constraints on the marginalised $\chi^2(\sigma_{v,1}, \sigma_{v,2})$ distribution for a two-cluster model along line of sight through the centre of A902. The cluster positions have been marginalised over with the weak constraint that $z_1 < z_2 < 1$.

is the different weighting assigned to the galaxy shear values in these analyses. In Gray et al, where no redshifts were available, each galaxy was given equal weighting. Here we do have redshift information. Regardless of the number of galaxies, which varies from redshift bin to redshift bin, each bin here has received equal weighting. Hence more weight is given to outliers, such as the $z = 1$ bin in A902, which pulls the mass estimate down.

The lesson we can conclude from this cluster analysis of masses and positions is the difficulty that a global, parametric fit may encounter when applied to real data. The positions of clusters in redshift is especially sensitive to any sharp variations in the amplitude of the shear. This is due to the fact that additional clusters are only detected in such a fit by appearance of jumps in the shear amplitude. Hence our analysis for the *positions* of two projected cluster along the line of sight in the direction of A902 is not conclusive and so the overall analysis is improved by the addition of redshift information for the lensing galaxies. However, the determination of the velocity dispersions is better, so long as we enforce a weak or strong prior on the cluster positions. While this demonstrates that some useful constraints on the parametric cluster masses can be extracted, even with current shear and photometric data, the problems encountered in this analysis suggest that a non-parametric approach to cluster finding and characterisation may also be worth investigation. In the next section we turn to reconstructing the full 3-D dark matter gravitational potential from our data.

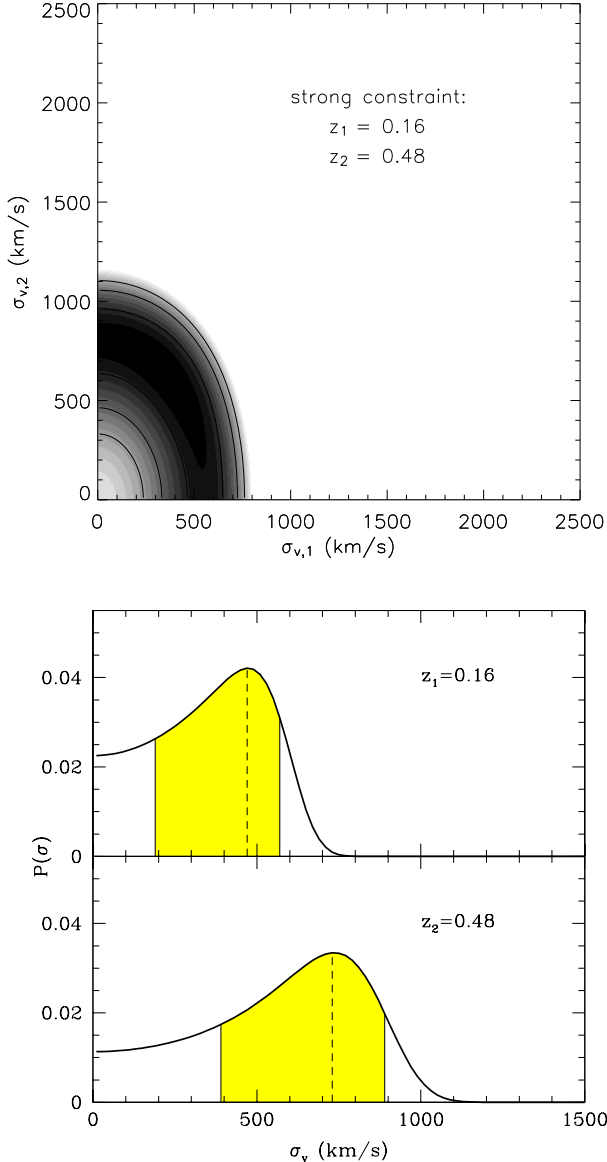


Figure 8. *Top:* Contours of 68%, 95% and 99.5% confidence constraints on the $\chi^2(\sigma_{v,1}, \sigma_{v,2})$ distribution for a two-cluster model along line of sight of A902 centre. Here we have assumed a strong prior by fixing the known cluster redshifts. *Bottom:* Probability distributions for each cluster velocity dispersion, marginalizing over the other cluster mass. The shaded regions indicate the 68% confidence regions.

5 RECONSTRUCTING THE 3-D DARK MATTER POTENTIAL

So far, we have used photometric redshifts to interpret our shear estimates as a 3-D shear field, and found we can constrain the redshifts and masses of clusters, and even possibly find evidence for a more complex line-of-sight density distribution. However, as we described in Section 2, we are now in a position to fully reconstruct the 3-D gravitational potential using a Kaiser-Squires (1993) inversion followed by the Taylor (2001) potential reconstruction method. In this section, we will use these methods to calculate the gravitational

potential for the A901/2 volume of space. This comoving volume is approximately $\theta^2 r^3 / 3 = 3 \times 10^5 [h^{-1} \text{Mpc}]^3$.

As discussed in Bacon & Taylor (2003), the intrinsic ellipticities of galaxies, σ_γ , create the major source of noise upon the gravitational potential reconstruction. In order to partially overcome this uncertainty, we average the shear estimators for many galaxies in a cell, chosen to have size $1.5' \times 1.5' \times \Delta z$ with redshift bin width $\Delta z = 0.05$; further smoothing can be applied if necessary at a later stage. We examine galaxies with $0 < z < 1$; galaxies with higher redshifts or no redshift assigned are all included in the final $z = 1$ bin. The full grid size is therefore $20 \times 20 \times 20$ cells.

5.1 The 3-D lensing potential

In order to calculate the gravitational potential, we must first determine the lensing potential from the shear field according to equation (6). We estimate this by taking the Fourier transform of the shear field and using the optimal weighting of Kaiser & Squires (1992) to find the Fourier transform of the lensing potential for each redshift slice;

$$\hat{\phi}(\mathbf{k}) = 2(\hat{k}_x^2 - \hat{k}_y^2)\gamma_1(\mathbf{k}) + 4\hat{k}_x\hat{k}_y\gamma_2(\mathbf{k}). \quad (35)$$

After an inverse Fourier transform to recover $\hat{\phi}(r, r\theta)$, we calculate the coefficients $\psi_{mn}(r)$ from equation (11) and correct the inversion for mean, gradient and paraboloid terms, as described in Section 2.2, yielding an estimate of $\Delta\phi$ at each slice in redshift.

We can estimate the uncertainty in a reconstruction of $\Delta\phi$ from the shot-noise estimates derived by Bacon & Taylor (2003), assuming an intrinsic ellipticity of $\sigma_\gamma = 0.3$:

$$\langle \Delta\phi^2 \rangle_{\text{SN}} = 1.7 \times 10^{-15} \left(\frac{n_2}{30/[1']^2} \right)^{-1} \left(\frac{\Theta}{1^\circ} \right)^2 \left(\frac{R^3}{z^2 \Delta z} \right), \quad (36)$$

where n_2 is the projected number density of lensed galaxies, R is the depth of the survey, and Θ is the angular radius of the survey. With the parameters of the COMBO-17 survey this becomes

$$\Delta\phi_{\text{rms}} \approx 5.5 \times 10^{-7} (z/0.1)^{-1}. \quad (37)$$

This is a reasonable estimate of the noise level we find in the A901/2 field, e.g. $\Delta\phi = 3.45 \times 10^{-7}$ at $z = 0.15$. However this underestimates the noise by a factor of 3.2 at $z = 0.5$, due to the assumption of a constant space density of galaxies.

Figure 9 shows two cross-sections of the reconstructed 3-D gravitational lensing potential, $\Delta\phi$, field after line-of-sight Gaussian smoothing with a filter scale of $\Delta z = 0.15$. We see in the top panel that the clusters are individually resolved in the transverse dimensions of the $\Delta\phi$ -field, shown at $z = 1$ where the signal-to-noise is highest. We have overlaid the field with a contour from the 3-D luminosity density (see Section 5.5) at $L = 8 \times 10^{10} L_\odot [h^{-1} \text{Mpc}]^{-3}$, indicating a strong correlation between the lensing potential and luminosity density. Individual 3-D pixels containing supercluster members have signal-to-noise of 1.5 to 2.1 between $z = 0.7$ and $z = 1$. We have already seen in Section 4 how such pixels can be integrated to obtain precise measurements of the mass of the clusters; here we will continue with moderate signal-to-noise pixels in order to reconstruct the gravitational potential. In the bottom panel, the typical ‘shark-fin’

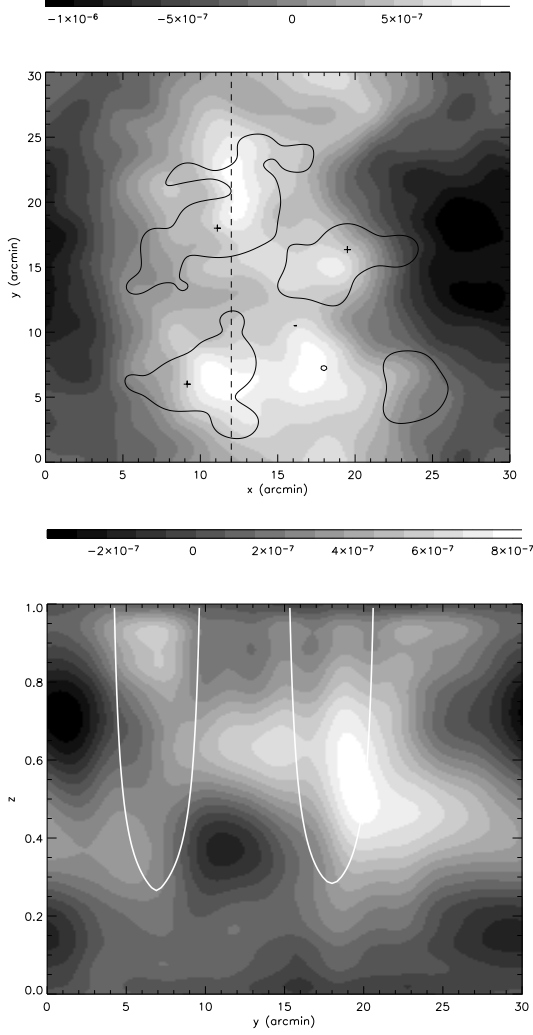


Figure 9. Cross-sections of the lensing potential, ϕ , for the A901/2 supercluster field. Top panel: (x, y) slice through $z = 1$, by which redshift the lensing potential arising from the clusters has grown substantially; note the clear detection of the three cluster signatures (luminosity peaks marked with crosses, luminosity density contour $L = 8 \times 10^{10} L_{\odot} [h^{-1} \text{Mpc}]^{-3}$). Bottom panel: (y, z) slice through $x = 12'$; this is a slice through A901a and A902. Note the growth of the lensing potential signal with redshift behind the two clusters. Solid lines show theoretical contours of ‘shark-fin’ growth at these cluster positions).

behaviour of the lensing potential behind the A901/2 supercluster can be clearly seen; $\Delta\phi$ grows with redshift behind the supercluster members.

5.2 Reconstructing the 3-D gravitational potential

We can now use equation (15) to reconstruct the 3-D gravitational potential, Φ . Following Bacon & Taylor (2003), we approximate derivatives in the redshift direction by second-order differences to reduce error propagation;

$$\partial_z \phi(\mathbf{r}) = \frac{\phi(x, y, z - \Delta z) - \phi(x, y, z + \Delta z)}{2\Delta z}, \quad (38)$$

and

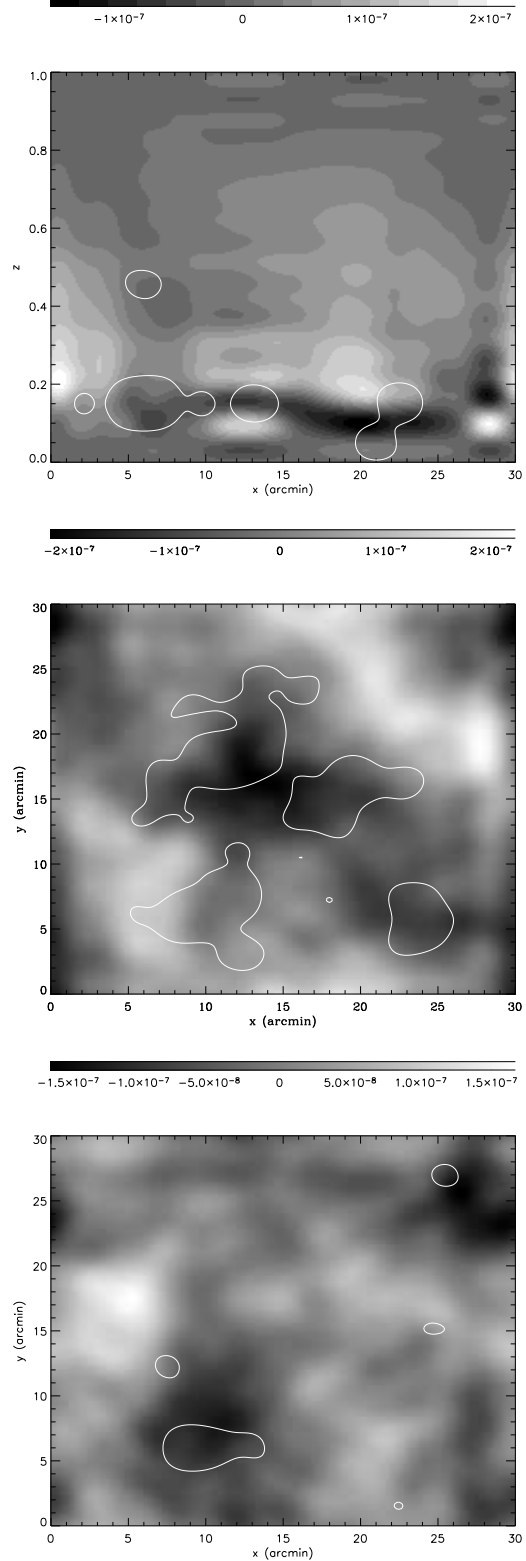


Figure 10. Cross-sections of the 3-D gravitational potential, Φ , for the A901/2 supercluster field. Top panel: (x, z) slice through $y = 12'$. The gravitational troughs at $z \simeq 0.15$ is associated with the supercluster (luminosity peaks marked with crosses, luminosity density contour $L = 3 \times 10^{10} L_{\odot} [h^{-1} \text{Mpc}]^{-3}$). Note also the trough at $z \simeq 0.45$, corresponding to a mass concentration CB1 detected behind A902. Middle panel: (x, y) slice through the $z = 0.15$ to 0.2 slice. We see the troughs associated with the supercluster members (luminosity density contour $L = 8 \times 10^{10} L_{\odot} [h^{-1} \text{Mpc}]^{-3}$). Bottom panel: (y, z) slice through $x = 12'$ to 0.5 . Note the trough associated with the background cluster CB1 (luminosity density contour $L = 2 \times 10^{10} L_{\odot} [h^{-1} \text{Mpc}]^{-3}$).

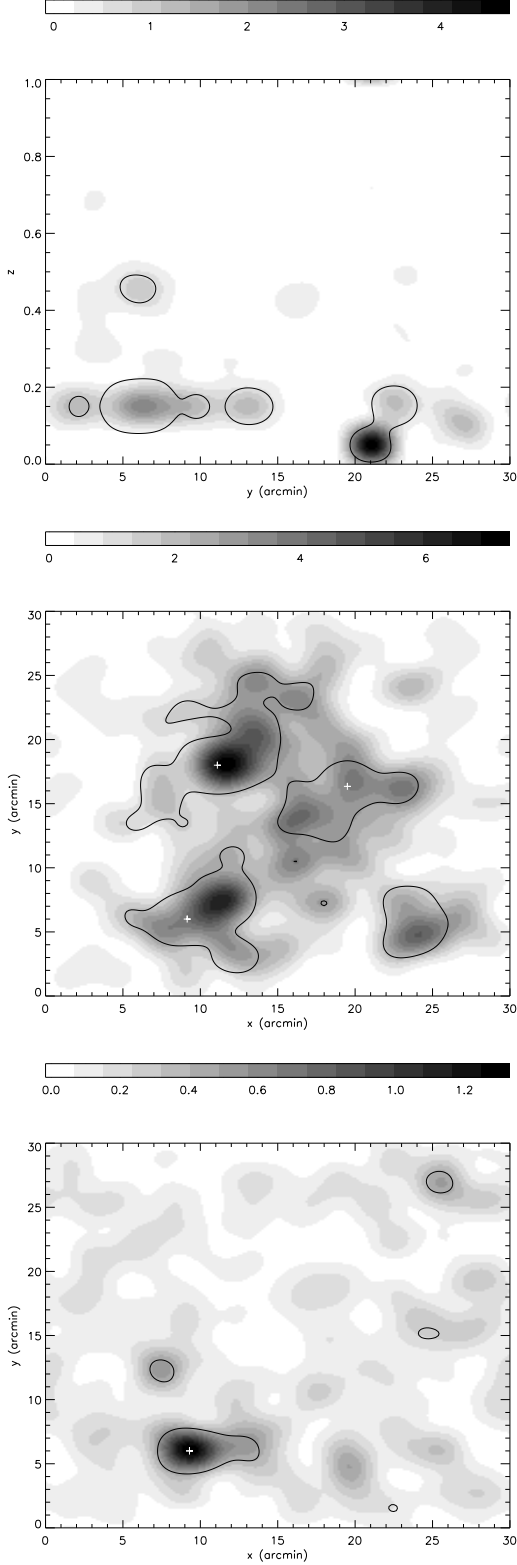


Figure 11. Cross-sections of the 3-D galaxy number density n for the A901/2 supercluster field. Slices and luminosity contours correspond to those in Fig. 10. Note the overdensities due to the supercluster at $z = 0.16$ and the mass concentration CB1 at $z = 0.48$.

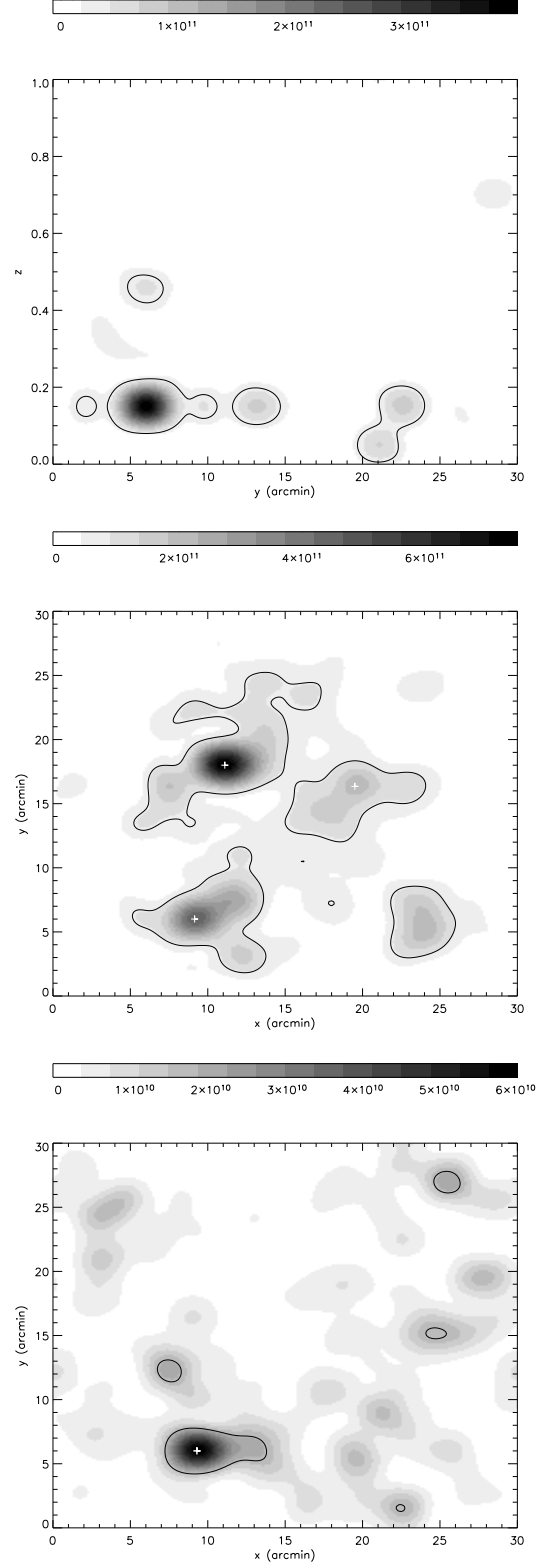


Figure 12. Cross-sections of the 3-D luminosity density for the A901/2 supercluster field. Slices correspond to those in Fig. 10. Note the overdensities due to the supercluster at $z = 0.16$ and the mass concentration CB1 at $z = 0.48$.

$$\partial_z^2 \phi(\mathbf{r}) = \frac{\phi(x, y, z - \Delta z) + \phi(x, y, z + \Delta z) - 2\phi(x, y, z)}{(\Delta z)^2}, \quad (39)$$

where Δz is the width of a bin in redshift.

The expected signal-to-noise for the potential field can be estimated from the analytic results of Bacon & Taylor (2003) who found that the shot-noise contribution was

$$\langle \Phi^2 \rangle_{\text{SN}} = 2.5 \times 10^{-16} \left(\frac{n_2}{(30/[1'])^2} \right)^{-1} \left(\frac{\Theta}{1''} \right)^2 \left(\frac{z}{\Delta z} \right)^4 \left(\frac{R}{\Delta z} \right), \quad (40)$$

where $\Delta z = 0.05$ is the size of redshift bin. For the COMBO-17 survey we find

$$\Delta \Phi(z) = 8.5 \times 10^{-8} (z/0.1)^2, \quad (41)$$

compared with an expected signal of $\Phi \sim 10^{-7}$. Since this implies a signal-to-noise of near unity, we must Wiener filter to proceed further; we Wiener filter the resulting Φ -field in the z -direction according to equation (18). This completes the process of obtaining a measurement of the 3-D Φ -field with reasonable signal-to-noise; we are now able to examine our resulting maps.

5.3 Mapping the potential

Figure 10 shows three cross-sections through the final, Wiener filtered Φ -field. We note several significant features of this field. The top panel of Figure 10 shows a slice in the (y, z) plane through $x = 12'$, of the supercluster potential. As for the lensing potential, we have overlaid this with a contour from the 3D luminosity density (see Section 5.5) at $L = 3 \times 10^{10} L_\odot [h^{-1} \text{Mpc}]^{-3}$. The gravitational potential well associated with supercluster A901/2, at $z = 0.16$, is clearly recovered with a peak pixel S/N of 2.7. The cluster centres of A901a and A902 are also visible clearly visible in this slice.

Beyond the supercluster, the potential field rises as we enter a void. But beyond that, at $z \simeq 0.48$, there is clearly a second mass concentration, corresponding to the luminosity peak of the background cluster CB1 behind A902. This has a peak Φ pixel S/N of 3.5, and is therefore actually more significant per pixel than the supercluster itself. This is consequently the first 3-D gravitational potential reconstruction of a cluster behind another cluster.

The position of CB1 is reasonably well constrained from the galaxy number distribution (see Section 5.4); $z = 0.48 \pm 0.1$. Bacon & Taylor (2003) find that the Wiener filtering only biases the position of structure by $\Delta z \simeq 0.05$ with ground-based noise levels, which is consistent with the small offset seen in the position of the minimum of the CB1 potential well. Hence our non-parametric map-making approach has succeeded in finding and deprojecting clusters in the shear field, substantially improving upon a parametric fit to the raw shear data. However the absolute depth of the potential well is not so well determined, as the Wiener filter will bias this by a factor $\sim S/(S+N)$ (equation 18). Hence, once a cluster is detected and its position is determined, a parametric fit is required to estimate its mass. These mass estimates are presented in Table 1, for both single and double clusters models, with the redshifts given by the galaxy number counts.

The middle panel of Fig. 10 shows a slice in the (x, y) -plane at $z = 0.15$ to 0.2 , the redshift bin including the su-

percluster, overlaid with a contour from the 3-D luminosity density at $L = 8 \times 10^{10} L_\odot [h^{-1} \text{Mpc}]^{-3}$. We see that the reconstructed gravitational potential wells correspond well to the positions of the three component clusters of A901/2. We will assess this quantitatively in Section 6. In this slice A901a has a peak pixel S/N of 2.7; A901b also has peak pixel S/N of 1.6, while A902 has peak pixel S/N of 1.4.

The bottom panel of Fig. 10 shows a second slice at $z = 0.45$, corresponding to the position of the second structure, overlaid with a luminosity density contour $L = 2 \times 10^{10} L_\odot [h^{-1} \text{Mpc}]^{-3}$. Again we see that the minimum of the potential well lies close to that of the background cluster CB1's luminosity peak. The peak signal-to-noise of CB1's gravitational potential is 3.5, constituting a secure detection with our map.

Figure 13 (upper panels) shows a 3-D image of the dark matter potential field of the A901/2 supercluster and CB1. The coordinates are $(x, y, z) = (\theta_x, \theta_y, z)$, which introduces some distortion. The left-hand panel shows a view of the supercluster field seen from high-redshift, looking back in the direction of the observer. Hence the positions of the supercluster centres is flipped left-to-right compared with the middle panels of Figure 10. The axis of the 3-D plot are in pixel units, with scaling $\Delta x = -1.5$ arcmin, $\Delta y = 1.5$ arcmin, and $\Delta z = 0.05$ in redshift. The main features of the supercluster are clearly identified, with the peak of the cluster luminosities at A901a at $(x, y) = (12, 11)$ (in pixel units), A901b at $(7, 10)$ and A902 at $(13, 5)$. Here A902 is below our threshold and so does not appear. The lower feature, centered at $(10, 5)$ is the background cluster CB1. Two other potential wells appear at $(5, 5)$ and $(1, 4)$, which also have galaxy counterparts. The right-hand panel is an oblique view of the supercluster, with the $x - y$ axis at the bottom and the vertical z -axis. The main A901/2 supercluster complex is clearly seen as a sheet mass distribution, although there is some leakage of the potential field to slightly higher redshift from the main A901a/b complex. This is most probably due to the radial Wiener filtering of the field. The CB1 cluster is clearly seen as a separate structure at higher redshift, $z = 0.48$.

5.4 The galaxy number density distribution

We can compare our results on the 3-D dark matter potential field with the visible matter distribution, traced by the galaxy number density. To estimate this we use the full galaxy redshift catalogue for the A901/2 field, i.e. all galaxies with photometric redshifts, rather than only the galaxies used for our shear analysis. This provides a total of 15147 galaxies with photometric redshifts. The galaxy count for each cell in the 3-D grid is then determined. Using the results of Wolf et al (2003) for the COMBO-17 survey, we possess an estimate for each cell of the incompleteness of the galaxy count. For $z < 0.8$, the counts are 90% complete. In the analysis below, we correct our galaxy counts by the incompleteness measure as a function of magnitude, redshift and spectral type (c.f. Wolf et al 2003). We further introduce an absolute magnitude threshold of $M_B < -19.5$ in order to counter the effect of seeing many low-luminosity galaxies at low redshift.

Figure 11 shows the Gaussian-smoothed ($\Delta\theta = 1.5'$, $\Delta z = 0.05$) galaxy number density in the same volume

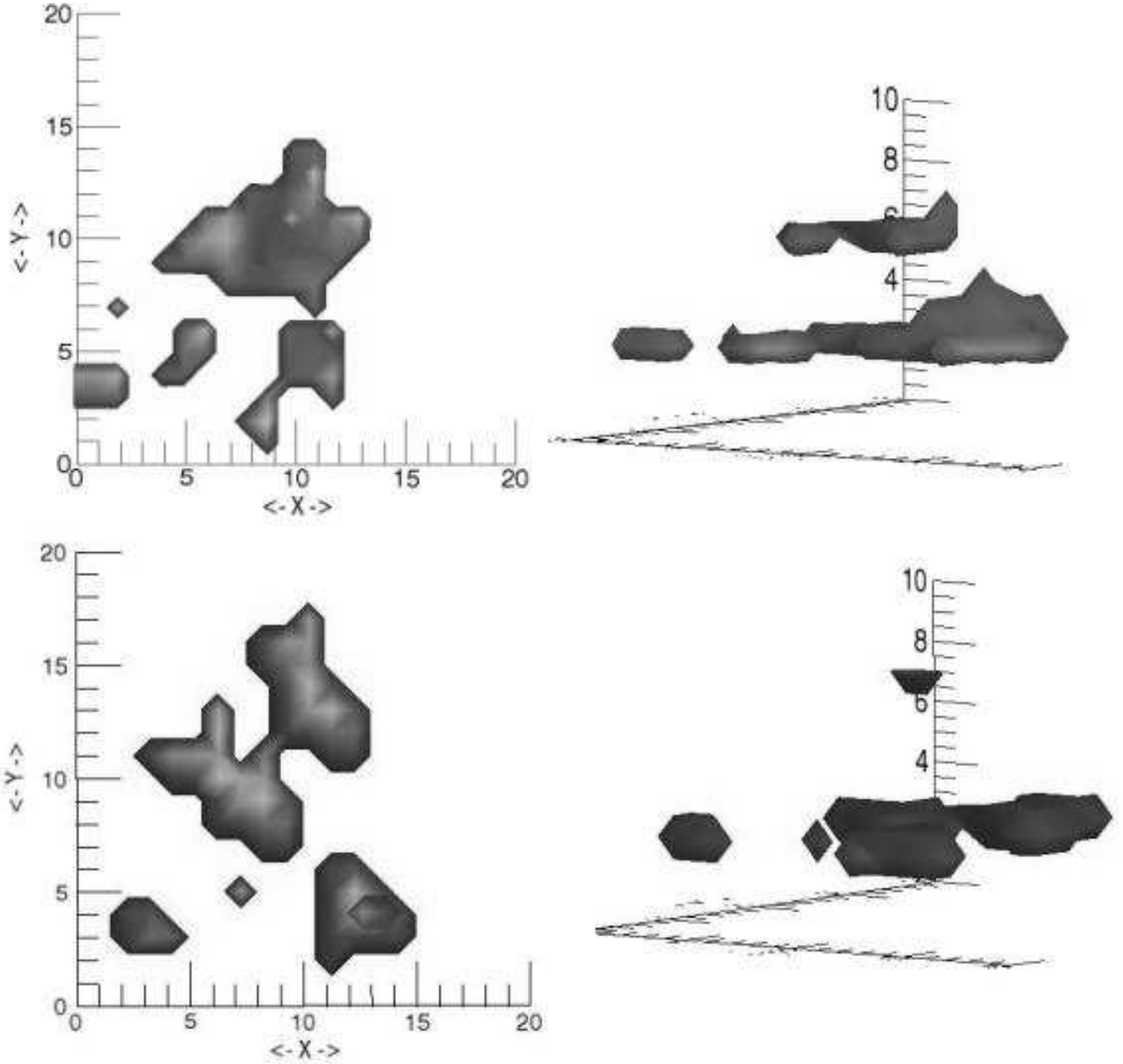


Figure 13. Three-dimensional iso-surface plots of the dark matter potential and galaxy number density fields. The coordinates of the map are $(x, y, z) = (\theta_x, \theta_y, z)$, which distorts the map geometry (note axis are in pixel units, where $\Delta x = \Delta y = 1.5$ arcmins and $\Delta z = 0.05$ in redshift). **Upper panels:** (LHS) The dark matter potential field, seen from high-redshift looking back to $z = 0$ and (RHS) at an oblique angle. The supercluster A901/2 is seen as a sheet in the potential field in the lower part of the RHS map. The new cluster CB1 is clearly seen as an isolated structure in the potential field behind A902 at $z = 0.48$. A902 is at a lower threshold and not plotted. **Lower panels:** (LHS) The galaxy number density field for the A901/2 field, in the same projection as the above dark matter image, and (RHS) in oblique projection. The main overdensities due to the supercluster are seen as a sheet at low redshift, while the CB1 cluster is clearly seen at $z = 0.48$.

of space as our gravitational potential. The top panel again shows a slice in (y, z) , and again we see the galaxy excess due to the A901/2 supercluster at $z = 0.16$. There is also a peak in the number counts at $z = 0.48$ at the position of the background cluster CB1. The middle panel of a slice at $z = 0.15$ shows up the three cluster cores, while the bottom panel slice at $z = 0.45$ shows CB1 as the most significant galaxy number density at that redshift. Thus we see that one approach to studying significant mass concentrations is to detect clusters using number counts, and compare with gravitational potential maps. Conversely, Φ maps may lead to further scrutiny of number density maps to find visible counterparts to potential wells.

Figure 13 (lower panels) again shows a 3-D image, in $(x, y, z) = (\theta_x, \theta_y, z)$ coordinates, of the iso-number density surface of the A901/2 supercluster and CB1. The left-hand panel shows the same viewing angle as the above dark matter potential, and so the cluster positions are again flipped left-to-right compared with the middle panel of Figure 11. The main clusters, A901a, A901b and A902 are all clearly visible at this threshold, and there is some evidence for another new cluster again at $(x, y) = (3, 3)$ in pixel units. The new cluster CB1 is seen in projection in front of A902 at $(13, 4)$. The right-hand panel shows the same image rotated to an oblique projection, with the x - y plane at the bottom, with the vertical z -axis. Again the A901/2 supercluster galaxy number density forms a distinct sheet at low redshift, while the CB1 cluster is again clearly visible at a higher redshift behind A902. Note that the redshift of CB1 seen in number density is slightly higher than that of the dark matter potential well. This slight shift is again probably due to Wiener filtering of the dark matter potential field.

5.5 The galaxy luminosity-density distribution

Finally, we also compare the dark matter potential with the 3-D luminosity density. In order to do this, we use the absolute magnitudes, M_{abs} , estimated by Wolf et al (2002) for all galaxies with redshifts. The luminosity, $L = 10^{-0.4(M_{\text{abs}} - M_{\odot})} L_{\odot}$ where M_{\odot} is the solar magnitude, is calculated for each galaxy. Using the same grid as before ($3' \times 3' \times [\Delta z = 0.05]$ cells), the luminosity is summed for each cell. Again we apply the completeness correction of Wolf et al (2003) as a function of magnitude, redshift and spectral type, plus an absolute magnitude cutoff of $M_B < -19.5$.

Fig. 12 shows cross-sections through the 3-D luminosity density corresponding to the same slices as in Fig. 10, with Gaussian smoothing of $1.5'$, $\Delta z = 0.05$ applied. Again the top panel shows significant peaks in the luminosity for the supercluster at $z = 0.16$ and CB1 at $z = 0.48$. The middle panel shows the three peaks of the A901/2 supercluster clearly. As seen above, there appears to be good agreement between the mass and light; we will quantify this in Section 6. The luminosity we measure within a comoving aperture of $0.5 h^{-1} \text{Mpc}$ for each member cluster is presented in Table 1. We also estimate the mass-to-light ratio for each of these clusters.

The bottom panel in Fig. 12 shows a slice in x and y at $z = 0.45$, the redshift bin including CB1. Here we find the expected luminosity peak. Again we present the mea-

sured luminosity, and mass-to-light ratio of CB1 within a comoving aperture of $0.5 h^{-1} \text{Mpc}$ in Table 1.

5.6 Comparison with a 2-D lensing analysis

We summarize the results of our 3-D lensing analysis in Table 1, which shows the redshift, velocity dispersion, mass, luminosity and the cluster mass-to-light ratio within $0.5 h^{-1} \text{Mpc}$ of each cluster centre, for A901a, A901b, A902 and CB1. The redshifts are taken from the galaxy number density, while the velocity dispersions, and hence masses, are estimated from the parametric fits to a single-cluster model in Section 4.1 for A901a and A901b, and the two-cluster fit of Section 4.2 for A902 and CB1. Note that in this latter case, the cluster masses are not independently determined. These may be compared, to some extent, with the 2-D shear analysis of Gray et al (2002).

The addition of redshift information has altered the measured masses of all three clusters relative to the 2-D analysis of Gray et al (2002); A901a mass has increased by a factor 2.8 in a $3'$ aperture, while A901b has decreased its mass by 40%. But of most interest is the behaviour of A902: in Gray et al (2002) the projected mass within an aperture of radius $0.5 h^{-1} \text{Mpc}$ from the centre of A902 is $16.7 \times 10^{13} M_{\odot}$ (see again Figure 11, Gray et al (2002)). In our 3-D analysis, and after deprojection with CB1, we find that A902 drops to a mass of $M = 5.1^{+2.4}_{-4.3} \times 10^{13} M_{\odot}$.

While it is tempting to assume that this drop is due to the deprojection of A902 with CB1 (and the fact that this can be done is clearly an advantage of the 3-D lensing approach), in this case the main cause is due to the different weighting of shear data. In the 2-D case shear was weighted per galaxy, while in the 3-D case it is weighted per redshift bin. This means the data is susceptible to bias by outliers. In the case of A902, there is a clear low outlying shear bin at $z = 1$ which, though containing relatively few galaxies, pulls the cluster mass down by a factor of two compared to the shear at higher redshift. This effect can also be seen in the single cluster model, but could be combated with a larger dataset (e.g. with number densities expected from space-based observations) and different weighting of redshift bins. We conclude that although with 3-D lensing we are able to measure a large mass for CB1, a cluster of that mass at $z = 0.5$ is not a significant contaminant to the 2-D shear signal of a foreground structure at $z = 0.16$. This can be seen from the fact that the measured mass of A902 drops only slightly in Table 1 as we move from a one-cluster to two-cluster analysis.

Luminosities for the clusters have increased substantially (by a factor $\simeq 3$) from the analysis of Gray et al (2002); this is because the previous study looked at early-type galaxies only, and had no means of applying a correction for undetected luminosity.

After these changes, and despite the removal of projection effects, there is still no simple relationship between mass and light in the A901/2 system, suggesting that it is not in a dynamically settled state. However, the variation in mass-to-light in A901/2 is now only by a factor of 2 from cluster to cluster, rather than the factor of 5 in the previous study.

In this section we have presented 3-D maps of the gravitational dark matter potential, the smoothed galaxy number

model	Cluster	z	σ_v (km s^{-1})	$M(< 0.5 h^{-1}\text{Mpc})$ ($\times 10^{13} M_\odot$)	$L(< 0.5 h^{-1}\text{Mpc})$ ($\times 10^{11} L_\odot$)	M/L ($\times M_\odot/L_\odot$)
one cluster	A901a	0.16	680^{+25}_{-90}	$10.8^{+0.8}_{-2.7}$	24.7	43.7
	A901b	0.16	600^{+40}_{-85}	$8.4^{+1.2}_{-2.2}$	13.5	62.2
	A902	0.16	520^{+55}_{-90}	$6.3^{+1.4}_{-2.0}$	19.5	32.3
two clusters	A902	0.16	470^{+100}_{-280}	$5.1^{+2.4}_{-4.3}$	19.5	26.2
	CB1	0.48	730^{+160}_{-340}	$12.0^{+6.0}_{-8.9}$	13.0	92.3

Table 1. Parameters of the four clusters in the COMBO-17 A901/2 supercluster field. We have assumed $h = 0.72$ in these estimates. The cluster velocity dispersions and mass estimates are from the parametric fits of Section 4.1 for a single cluster model, and Section 4.2 for a double cluster model, with the cluster redshifts fixed at the positions given by the galaxy number counts.

counts and the luminosity density. In order to quantify these distributions further we now calculate the statistical correlations between these quantities, and compare then with the predictions from the halo model.

6 MASS-GALAXY CORRELATIONS

Now that we have estimated the 3-D gravitational potential in the A901/2 field we are in a position to examine the auto- and cross-correlations functions of the 3-D gravitational potential, the galaxy number density and the galaxy luminosities. In this Section we describe the procedure used to calculate these correlation functions and briefly interpret our results. We compare our results with the halo model developed in Section 2.5.

We calculate the auto- and cross-correlations using equation (19) where the average is taken over all cell pairs in each slice in redshift bins which are separated by r_\perp . Having calculated the auto- and cross-correlation functions for each redshift slice, we take the mean of these correlation functions to measure the overall correlation functions in 3-D (the physical distance between slices is too large for substantial correlations). As a simple estimate of the uncertainty, we use $\sigma_{\text{slice}}/\sqrt{N_z}$, where σ_{slice} is the standard deviation of the slice correlation functions and N_z is the number of slices. This acts as a better measure of the uncertainty than the standard deviation of correlations for all pairs, as pairs in a given slice have highly correlated values for the correlation function.

6.1 The gravitational potential auto-correlation

The gravitational auto-correlation function, $C^{\Phi\Phi}(r)$, is shown in Figure 14. This shows that the variance at zero separation is $\langle\Phi^2\rangle \approx 2 \times 10^{-15}$, implying that $\Phi \sim 5 \times 10^{-8}$, averaged over cells of size $1.5' \times 1.5' \times \Delta z = 0.05$. It should be born in mind that the Wiener filtering in the redshift direction will affect the amplitude of the reconstructed potential field (Hu & Keeton, 2003; Bacon & Taylor, 2003). Here we have chosen a Wiener filter which reproduces the masses inferred from the parametric fits found in Section 4.

The measured potential correlation drops rapidly within $r \sim 2 h^{-1}\text{Mpc}$, then becomes slightly negative before going to zero at $r \approx 6 h^{-1}\text{Mpc}$. As the mean of the potential field is zero in each redshift slice, there is a constraint which forces the integral of the correlation function to be zero over the

field. Hence a positive correlation at small scale must be compensated by a negative correlation at larger separation.

As discussed in Section 2.5, the halo-model provides an estimate of the theoretical potential correlations, ensemble averaged over the whole mass range of collapsed objects. The lighter solid line in Figure 14 shows the expected potential-potential correlation function for all halo masses in a survey of the size and depth of the A901/2 field, and with the same pixelisation, and the same integral constraint as our reconstructed data.

The amplitude at zero separation agrees with the data in the A901/2 field, although this has been modified by the Wiener filter to match the cluster velocity dispersions. However the predicted correlations are higher at larger separation than the data. The halo model correlation function then passes through zero at a separation of around $r = 5.5 h^{-1}\text{Mpc}$ due to the integral constraint.

In such a finite survey, the high-mass end of the mass function is not well sampled, as very high-mass peaks appear only rarely in such a small survey. To account for this, we have also evaluated the theoretical correlations over a truncated mass range, up to the mass cut-off of the survey. In the case of the A901/2 field we truncate the mass range at $M = 10^{13} M_\odot$, corresponding to the mass of the main clusters. The dark solid line is the halo-model expectation value of the potential correlation function with this mass truncation. With the mass range truncated the amplitude of the potential correlations drops to around $\langle\Phi^2\rangle \approx 4 \times 10^{-16}$, before slowly dropping to zero due to the integral constraint.

The shape of the halo-model potential correlations still does not fit the data from the A901/2 field well. As the gravitational potential is a long range force, we should expect it to survive to larger distances, until the integral constraint cuts in. However here we see that the measured 3-D potential drops rapidly to zero. There are two possible causes for this. The first is that the correlation function is dominated by the main clusters in the field, but that the mass in these clusters is highly concentrated in the cluster cores. However it is more likely that, while the correlation function is dominated by the main clusters, the reason for the shape decline is due to the finite field of view and the requirement that the mean of the field is zero at each redshift slice. This will cause us to lose longer-range correlations in the potential field. Although the halo model does take this integral constraint into account, it does so averaged over many realisations of the potential field, and so does not well match single clusters. In addition the potential reconstruction removes any long-

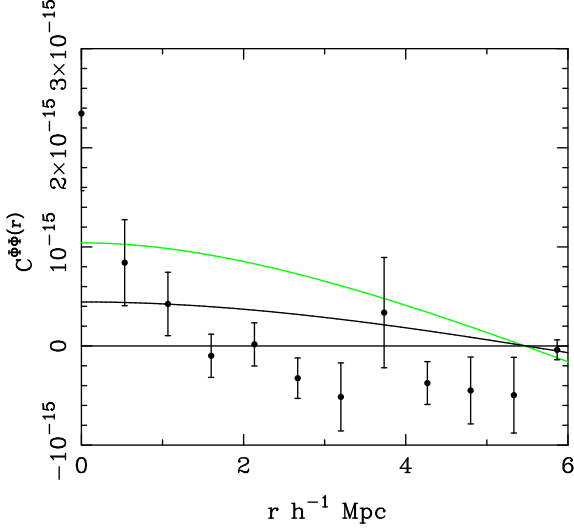


Figure 14. The auto-correlation function of the gravitational potential, Φ . Data points are from a correlation analysis of the A901/2 COMBO-17 field. The dark solid line is the prediction of the halo model, with a mass cut-off. The light solid line is the same prediction with no mass cut-off.

range potential gradient and quadratic modes in each redshift slice. However, if we averaged over a number of larger fields, we would expect the results to converge on the halo-model.

6.2 The galaxy number density auto-correlation

Figure 15 shows the auto-correlation function of the galaxy number density, $C^{nn}(r)$. In this case we have calculated the correlations between absolute number densities, $n(\mathbf{r})$, rather than fractional overdensities, to avoid sensitivity to the mean of the field, and so there is no integral constraint. Note that we have truncated the COMBO-17 catalogue at $m_B < -19.5$, to ensure we are selecting the same type of galaxies as in our model.

At $r = 0$ there is a positive correlation, with $C^{nn} \approx 0.04 [h^{-1}\text{Mpc}]^{-3}$ due to the galaxies within each cluster. This falls to zero as we move to separations wider than the clusters.

The halo model does a better job of fitting the data, as the number density of galaxies is a local property, although the scatter in the data is large. The lighter line in Figure 15 shows the number correlations for all halo masses, while the darker line shows the correlations for masses $< 10^{13} M_\odot$. Both are in agreement with the trend of the data.

Interestingly the correlations in the galaxy number density seem to have a longer scale-length than that of the potential. As discussed above there are two possible explanations for this. One is that the potential correlations are far shorter than implied by the galaxy number densities. If this is the case, the dark matter generating the potential must be very compact. However, it is more likely that this is again due to the subtraction of the mean potential in the field, applied to each redshift slice, and the removal of any gradient or parabolic part of the potential field. These are most likely causing us to miss part of the larger-scale potential field.

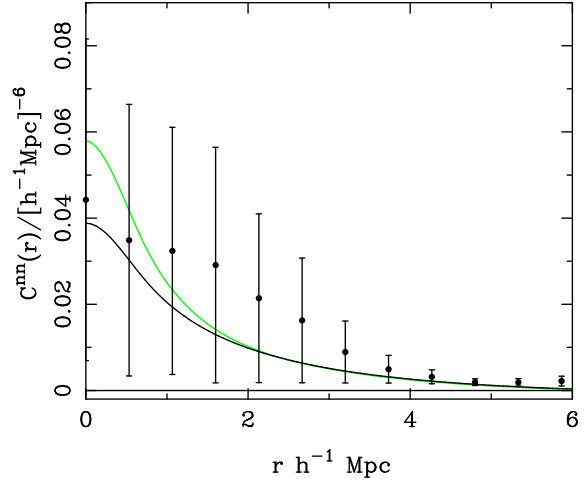


Figure 15. The auto-correlation of the number density n from the A901/2 field in the COMBO-17 data-set. Lines are the predictions of the halo model. The lighter line is for all halo masses, the darker line is for haloes with mass $< 10^{13} M_\odot$.

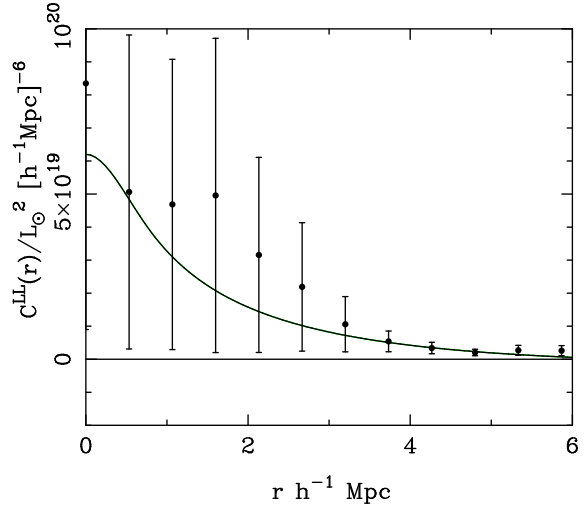


Figure 16. The auto-correlation function of galaxy luminosity density, L , from the A901/2 field in COMBO-17. As in the previous figures, the lines are predictions for the halo model.

6.3 The galaxy luminosity auto-correlation function

Figure 16 shows the galaxy luminosity density projected auto-correlation function, $C^{LL}(r)$. The COMBO-17 data points are positively correlated with $C^{LL} \approx 8 \times 10^{19} L_\odot^2 [h^{-1}\text{Mpc}]^{-6}$ at zero separation, implying that the luminosity density is $L \approx 10^{10} L_\odot [h^{-1}\text{Mpc}]^{-3}$ for galaxies in the A901/2 field with $m_B < -19.5$.

The amplitude at small separations is again dominated by the clusters, although the scatter is again large. Further out, the signal remains positive, until around $r = 3 h^{-1}\text{Mpc}$, when it dies away to zero. As with the galaxy number counts, there is no integral constraint on the luminosity densities.

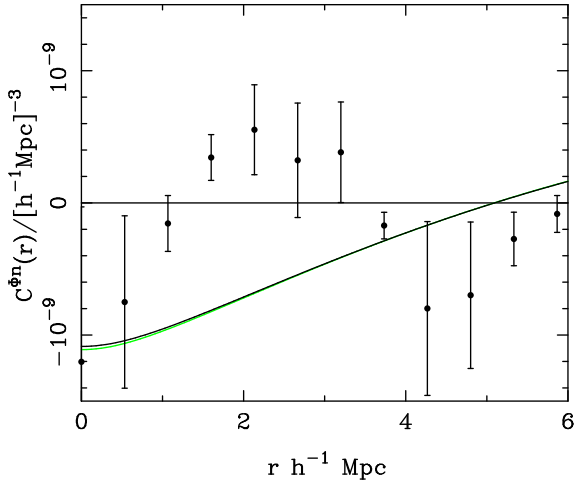


Figure 17. Cross-correlation of the gravitational potential Φ and number density n , $C^{\Phi n}(r)$. The solid lines are, as in previous figures, predictions from the halo model.

We have also calculated, for the first time, the prediction of luminosity densities from the halo model. Here again we see good overall agreement between the model and data. At small separation the model peaks at approximately the right amplitude, and then drops off with increasing distances. Interestingly, the halo model accounts for the drop-off at large separation very well.

6.4 The gravitational potential and the galaxy number density

Our estimate of the cross-correlation of the gravitational potential and the galaxy number density is shown in Figure 17. At $r = 0$ the signal is dominated by the correlations between the excess number of galaxies found at the bottom of the gravitational potential well, and shows a slight anti-correlation. On larger scales the cross-correlation starts to oscillate due to the dominance of the supercluster. This oscillation arises as we move out of the cluster centre and the gravitational potential increases to a maximum; we find a positive correlation at $r = 2.5 h^{-1} \text{Mpc}$ between the potential maximum and the galaxies in the potential wells. Moving further away, we move into the gravitational potential of a nearby cluster, and reach a second anti-correlation at $r = 4.5 h^{-1} \text{Mpc}$, the typical inter-cluster distance in the supercluster. On scales larger than $r > 5 h^{-1} \text{Mpc}$ we move out of the supercluster itself.

The predictions of the halo model correlations for all masses (light line) and for a mass cut-off (dark line) are also shown in Figure 17. This has little effect on the predicted correlation and the amplitude of the anti-correlation at small r again agrees with our measurement. The halo model does not contain the oscillations due to the dominance of the main clusters, indicating again that our sample is too small to converge to general predictions. The main discrepancy is the positive correlation at $r \approx 3 h^{-1} \text{Mpc}$. As the predicted galaxy number density correlations were in fair agreement with the COMBO-17 data we can conclude that the differ-

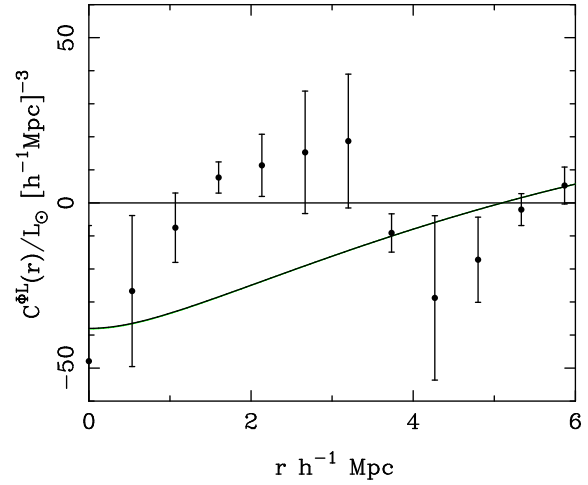


Figure 18. Cross-correlation of the gravitational potential, Φ , and luminosity density, L , $C^{\Phi L}(r)$. The solid lines are, as in previous plots, predictions from the halo model.

ence between data and theory lies with the correlations of the potential field (see Figure 14), which are not so well matched. However, as noted above, this is mainly due to the small field size compared with the structures we are mapping; the imposed zero mean of the gravitational potential at the supercluster slice has offset the $\Phi - n$ correlation, and this will be alleviated by using a larger field.

6.5 The gravitational potential and the galaxy luminosity

The $\Phi - L$ correlation function, $C^{\Phi L}(r)$, is calculated for each redshift slice in a similar fashion to the $\Phi - n$ correlation function. Again, the mean and variance of the correlation function found for different redshift slices is used to calculate the value and error on the overall correlation function. We show the $C^{\Phi L}$ correlation function in Figure 18.

We find only marginal evidence for an anti-correlation between potential and luminosity at small scales. However we might expect a high luminosity where there is a deep gravitational potential well, as suggested by the halo model. As with the potential-number density correlations, the cross-correlation of potential and luminosity density again rises to a positive value at around $r \approx 3 h^{-1} \text{Mpc}$. Again we can identify the discrepancy as being with the potential field, as we found fair agreement between the halo model predictions for luminosity-density correlations and the data. Once more, this will be alleviated by a larger field size.

7 CONCLUSIONS

In this paper we have for the first time measured the 3-D gravitational potential of a volume of space from gravitational lensing. This has been possible by accurately measuring the gravitational shear on the A901/2 supercluster field of the COMBO-17 survey, combining these shear measurements with photometric redshifts, and applying the re-

construction techniques of Kaiser & Squires (1993), Taylor (2001) and Bacon & Taylor (2003). We have described the COMBO-17 survey, including our measurements of weak shear (Gray et al 2002) and the photometric redshift accuracy of the survey, $\Delta z = 0.05$ for $0 < z < 0.8$.

As a first step towards full 3-D analysis of the A901/2 field, we have measured the tangential shear around the supercluster members as a function of redshift. By fitting a singular isothermal sphere shear model to the shear pattern behind each of these clusters (c.f. Wittman et al 2001, 2002) we estimated the clusters' velocity dispersion and redshifts from weak lensing alone. We found best-fit two-parameter velocity dispersions and redshifts of $\sigma_v = 840^{+100}_{-105} \text{ km s}^{-1}$ and $z = 0.30^{+0.10}_{-0.16}$ for A901a, $\sigma_v = 840^{+170}_{-115} \text{ km s}^{-1}$, $z_{\text{lens}} = 0.37^{+0.14}_{-0.11}$ for A901b and $\sigma_v = 760^{+220}_{-200}$, $z_{\text{lens}} = 0.38^{+0.23}_{-0.20}$ for A902. These measurements are consistent with photometrically determined redshifts of the clusters, $z = 0.16$. If we fix the redshifts of the cluster to the photometric redshift of $z = 0.16$, we find $\sigma_v = 680^{+25}_{-90} \text{ km s}^{-1}$ for A901a; $\sigma_v = 600^{+40}_{-85} \text{ km s}^{-1}$ for A901b; and $\sigma_v = 520^{+55}_{-90} \text{ km s}^{-1}$ for A902. We have also compared with velocity dispersions of the clusters found from a 2-D lensing analysis (Gray et al 2002) and found good agreement. Any differences are easily understood as due to the different weighting of shear data.

Examination of the 3-D number density of galaxies revealed the existence of a cluster, CB1, at $z = 0.48$ behind the A902 cluster. This prompted us to investigate a two-cluster shear analysis for A902 which provided results consistent with the presence of this second cluster. Our initial two-cluster analysis failed to improve on the redshift estimates of the two clusters, due to the difficulty a global parametric fit to the data has in dealing with outlying shear values. However, by fixing the positions of the clusters, either with a weak prior by restricting the redshifts of the clusters to lie below $z = 1$, or with a strong prior of fixing the redshifts to the known cluster positions, the total mass of the two clusters was well determined, and each cluster velocity dispersion could be marginalised over to give $\sigma_{v,1} = 470^{+100}_{-280} \text{ km s}^{-1}$ for A902 and $\sigma_{v,2} = 730^{+160}_{-340} \text{ km s}^{-1}$ for CB1.

We have calculated the 3-D lensing potential, $\Delta\phi$, for this volume of space using the methods of Kaiser & Squires (1993) generalised to a 3-D grid. We have then used this lensing potential to reconstruct the 3-D gravitational potential, following the reconstruction method of Taylor (2001) and Bacon & Taylor (2003). To improve the signal-to-noise in the reconstructed potential field we Wiener filtered the potential field in the redshift direction, preserving the properties of the reconstructed field in the transverse direction.

The recovered gravitational potential was found to include the largest troughs at the positions of the supercluster members, with a peak signal-to-noise ratio at the central pixel of $S/N \approx 3$. Hence we have demonstrated that 3-D dark matter potential mapping is achievable with currently available shear and photometric redshift data, such as the COMBO-17 survey.

In addition to the A901/2 supercluster potential, a further significant (3σ per pixel) trough was found at $z = 0.48$ behind A902, corresponding to the background cluster CB1 seen in the 3-D number density and luminosity. This demonstrates that potential mapping will be a useful tool in the detection of clusters from lensing data, including clusters

behind clusters. Indeed this suggests an algorithm for the construction of a mass-selected cluster catalogue, which is free of projection effects. One first constructs a 3-D potential field from the shear and photometric data and searches for the largest potential wells. The positions of these clusters can be accurately determined from this galaxy number density field, while the cluster masses can be estimated from parametric fits.

Finally, we have developed the halo model to predict the auto- and cross-correlation functions of the 3-D potential field, the galaxy number density field and, for the first time, the galaxy luminosity-density field, taking into account the geometry of the survey and pixelisation. We compared these predictions with the measured auto- and cross-correlations between the gravitational potential and the galaxy number density, and between the gravitational potential and the 3-D luminosity distribution in the COMBO-17 A901/2 field. We found that peaks in the baryonic matter concentration were strongly correlated to troughs in the gravitational potential, as one would expect due to baryons preferentially being found at dark matter concentrations. We also found reasonable agreement between the amplitudes of the measured and predicted correlations – although the statistics of the A901/2 field are dominated by the four clusters. This introduces oscillations in the measured correlation functions as we move in and out of clusters. In particular, the correlation length of the potential field is shorter than we might have expected from the clustering of the galaxies. This is most likely due to the removal of the mean, gradients and parabolic terms in each redshift slice of the potential field, including the supercluster slice. This effect will be alleviated with larger area surveys (see Bacon & Taylor, 2003, for a further discussion of this effect).

In conclusion, the success of this study in measuring the 3-D gravitational potential bodes well for future 3-D lensing studies. We have seen that 3-D potential mapping will be useful for constructing mass-selected galaxy cluster catalogues with minimal projection effects. By extending and comparing with the halo model, we have also shown that the analysis of haloes within this framework can be extended to groups and clusters. With advent of better shear and photometric redshift data, from e.g. the SNAP survey (Massey et al 2003), the prospects look encouraging for 3-D mass mapping large volumes of the universe, to construct mass-selected cluster catalogues, to generate statistical probes of dark matter haloes over a wide range of scales, as a probe of cosmological parameters, and finally to compare the 3-D dark matter distribution with the properties of galaxies.

ACKNOWLEDGMENTS

ANT is supported by a PPARC Advanced Fellowship; DJB and MEG are supported by a PPARC Postdoctoral Fellowships. CW is supported by the PPARC Rolling Grant in Observational Cosmology at the University of Oxford. We thank Alan Heavens and Martin White for useful discussions.

REFERENCES

- Bacon D., Massey R., Refregier A., Ellis R.S., 2002, submitted to MNRAS, astro-ph 0203134.
- Bacon D., Taylor A.N., 2003, MNRAS, in press, astro-ph/0212266
- Bartelmann M., Schneider P., 2001, Phys. Rep., 340, 291.
- Bernstein G. M., Jarvis M., 2002, AJ, 123, 583.
- Bonnet H., Mellier Y., Fort B., 1994, ApJL, 427, 83.
- Brown M. L., Taylor A. N., Bacon D. J., Gray M. E., Dye S., Meisenheimer K., Wolf C., 2003, MNRAS, 341, 100
- Erben T., van Waerbeke L., Mellier Y., Schneider P., Cuillandre J.-C., Castander F. J., Dantel-Fort M., 2000, A&A, 355, 23.
- Gray M.E., Wolf C., Meisenheimer K., Taylor A.N., Dye S., Borch A., Kleinheinrich M., 2003, MNRAS, in press, astro-ph/0312106
- Gray M. E., Taylor A. N., Meisenheimer K., Dye S., Wolf C., Thommes E., 2002, ApJ, 568, 141.
- Gray M. E., Ellis R. S., Lewis J.R., McMahon R.G., Firth A.E., 2001, MNRAS, 325, 111
- Guzik J., Seljak U., 2002, MNRAS, 335, 311.
- Heymans C., Heavens A., 2002, accepted by MNRAS, astro-ph 0208220.
- Heymans C., Brown M., Heavens A.F., Meisenheimer K., Taylor A.N., Wolf C., 2003, submitted MNRAS
- Hoekstra H., Franx M., Kuijken K., Squires G., ApJ, 504, 636.
- Hoekstra H., Yee H., Gladders M., Barrientos L. F., Hall P., Infante L., 2002, ApJ, 575, 55.
- Hu W., 1999, ApJL, 522, 21.
- Hu W., Keeton C. R., 2003, submitted to PRD, astro-ph 0205412.
- Hu W., 2002, astro-ph 0208093.
- Huterer D., 2002, PhysRevD, 65.
- Jain B., Seljak U., 1997, ApJ, 484, 560.
- Jarvis M., Bernstein G., Jain B., Fischer P., Smith D., Tyson J.A., Wittman D., 2003, ApJ, 125, 1014
- Kaiser N., Squires G., 1993, ApJ, 404, 441.
- Kaiser N., Squires G., Broadhurst T., 1995, ApJ, 449, 460.
- Kaiser N., 1998, ApJ, 498, 26.
- King L., Schneider P., 2002a, accepted by A&A, astro-ph 0208256.
- King L., Schneider P., 2002b, A&A in press, astro-ph 0209474.
- Luppino G. A., Kaiser N., 1997, ApJ, 475, 20.
- Mellier Y., 1999, ARA&A, 37, 127
- Massey R. et al, 2002, in preparation.
- Peebles P. J. E., *Large-scale structure of the universe*, 1980.
- Pen U.-L., Lu T., van Waerbeke L., Mellier Y., 2003, MNRAS, submitted (astro-ph/0304512)
- Refregier A. R., Bacon D. J., 2002, MNRAS in press, astro-ph 0105179.
- Refregier A., Rhodes J., Groth E. J., 2002, ApJ, 572, 131.
- Rhodes J., Refregier A., Groth E. J., 2001, ApJ, 552, 85.
- Rhodes J., Refregier A., Groth E. J., 2000, ApJ, 536, 79.
- Seljak U., 1998, ApJ, 506, 64.
- Schindler, S., 2000, A&AS, 142, 433
- Squires G., Kaiser N., Fahlman G., Babul A., Woods D., 1996, ApJ, 469, 73.
- Taylor A.N., Dye S., Broadhurst T. J., Benitez N., van Kampen E., 1998, ApJ, 501, 539.
- Taylor A. N., 2001, submitted to Phys Rev Lett, astro-ph 0111605.
- Tyson J.A., Valdes F., Wenk R.A., 1990, ApJLett, 349, L1
- Umetsu K., Futamase T., 2000, ApJL, 539, 5
- van Waerbeke L., Mellier Y., Radovich M., Bertin E., Dantel-Fort M., McCracken H. J., Le Fevre O., Foucaud S., Cuillandre J.-C., Erben T., Jain B., Schneider P., Bernardeau F., Fort B., 2001, A&A, 374, 757.
- Weinberg K., & Kamionkowski M., 2002, MNRAS, 337, 1269
- White M., van Waerbeke L., Mackey J., 2002, ApJ, 575, 640
- Wittman D., Tyson J. A., Margoniner V. E., Cohen J. G., Dell'Antonio I. P., 2001, ApJ, 557, 89
- Wittman D., Margoniner V. E., Tyson J. A., 2002, submitted to ApJL, astro-ph 0210120
- Wolf C., Meisenheimer K., Röser H.-J., 2001, A&A, 365, 660
- Wolf C., Meisenheimer K., Rix H.-W., Borch A., Dye S., Kleinheinrich M., 2003, A&A, 401, 73